THE INFLUENCE OF DIFFERENT TRACER KINETIC MODELS IN ASSESSING THE EFFECT OF PHARMACOLOGICAL THERAPY OF MALIGNANT PLEURAL MESOTHELIOMA

Martina Vivoda Tomšič

Doctoral Dissertation
Jožef Stefan International Postgraduate School
Ljubljana, Slovenia

Supervisor: Assoc. Prof. Dr. Katarina Šurlan Popovič, Dr. Med., University Clinical Centre Ljubljana, Slovenia
Co-Supervisor: Assoc. Prof. Dr. Viljem Kovač, Dr. Med., Institute of Oncology, Ljubljana, Slovenia
Co-Supervisor: Assoc. Prof. Dr. Igor Serša, Jožef Stefan Institute, Ljubljana, Slovenia
Co-Supervisor: Prof. Sotirios Bisdas, Dr. Med., University College London Hospitals, London, United Kingdom

Evaluation Board:
Assoc. Prof. Dr. Boštjan Zalar, Chair, Jožef Stefan Institute, Jamova 39, Ljubljana, Slovenia
Assist. Prof. Dr. Martina Vrankar, Dr. Med., Institute of Oncology, Ljubljana, Slovenia
Prof. Dr. Đorđije Šaranović, Dr. Med., Faculty of Medicine, University of Belgrade, Serbia

MEDNARODNA PODIPLOMSKA ŠOLA JOŽEFA STEFANA
JOŽEF STEFAN INTERNATIONAL POSTGRADUATE SCHOOL

Martina Vivoda Tomšič

THE INFLUENCE OF DIFFERENT TRACER KINETIC MODELS IN ASSESSING THE EFFECT OF PHARMACOLOGICAL THERAPY OF MALIGNANT PLEURAL MESOTHELIOMA

Doctoral Dissertation

VLOGA RAZLIČNIH KINETIČNIH MODELOV PRI ANALIZI DINAMIKE SLEDILCA ZA OCENO UČINKOVITOSTI ZDRAVLJENJA MALIGNIH PLEVRALNIH MEZOTELIOMOV

Doktorska disertacija

Supervisor: Assoc. Prof. Dr. Katarina Šurlan Popovič, Dr. Med.

Co-Supervisor: Assoc. Prof. Dr. Viljem Kovač, Dr. Med.
Co-Supervisor: Assoc. Prof. Dr. Igor Serša
Co-Supervisor: Prof. Sotirios Bisdas, Dr. Med.

Ljubljana, Slovenia, March 2019

To my husband

Acknowledgments

This dissertation could not have been accomplished without the support of my supervisors Assoc. Prof. Dr. Katarina Šurlan Popovič, Dr. Med., Assoc. Prof. Viljem Kovač, Dr. Med., Assoc. Prof. Igor Serša and Prof. Sotirios Bisdas; to all of them I am most grateful. Assoc. Prof. Katarina Šurlan Popovič has proposed the research topic and has valuably guided me through all research phases, Prof. Sotirios Bisdas has helped me write the research proposal, kindly hosted me in Tubingen for the first analysis of MR data and helped extensively with article improvements. Assoc. Prof. Viljem Kovač has supported the clinical research and provided research guidance. Assoc. Prof. Igor Serša has helped with DCE-MRI protocol preparation, testing and improvements until it was suitable for patient scanning. All supervisors have systematically guided me through research planning and have helped me selflessly with the article and dissertation preparation.

In addition, I am also very thankful to the radiographers at the University Medical Centre Ljubljana, especially Andrej Sirnik for scanning the patients, Daniela Strbac, Dr. Med. from the Institute of Oncology for patient recruitment and clinical follow-up, and Prof. Peter Korošec.

I am also thankful to my family for their continued love and support.

The study was supported by the University Medical Centre Ljubljana research funding.

Abstract

Background: Malignant pleural mesothelioma (MPM) is a rare and aggressive thoracic malignancy that is difficult to cure and is linked to asbestos exposure. Dynamic contrast-enhanced magnetic resonance imaging (DCE-MRI) is a functional imaging technique used to analyze tumor microvascular properties and to monitor therapy response. The purpose of this study was to compare two tracer kinetic models, the extended Tofts (ET) and the adiabatic approximation tissue homogeneity model (AATH), for analysis of DCE-MRI and to examine the value of the DCE parameters to predict the response to chemotherapy in patients with MPM.

Method: This was a prospective, longitudinal and single-center study conducted between October 2013 and July 2015. Patients underwent DCE-MRI studies at three time points: pre-, intra- and post-chemotherapy. Images were analyzed using ET and AATH models. After finishing the chemotherapy, patients were classified as having disease control or progressive disease according to modified response evaluation criteria in solid tumors (mRECIST) criteria. Receiver operating characteristic curve analysis was used to examine specificity and sensitivity of DCE parameters for predicting response to therapy. Comparison tests were used to analyze whether derived parameters are interchangeable between the two models.

Results: Nineteen patients form the study population. The results indicate that the derived parameters are not interchangeable between the models. Significant correlation with response to therapy was found for AATH-calculated median pre-treatment efflux rate (k_{ep}) with estimated sensitivity of 83% and specificity of 100% (cut-off of ≥ 0.13 /min, AUC 0.92). ET-calculated maximal pre-treatment k_{ep} values showed a significant predictive value of MPM response during treatment with estimated 100% sensitivity and specificity (cut-off of ≥ 0.89 /min, AUC 1), but were less predictive for MPM response to therapy with estimated sensitivity and specificity of 83.3% and 92.3%, respectively ($P = 0.06$; cut-off of ≥ 1.31 /min, AUC 0.81).

Conclusions: The results of our study showed that ET and AATH models for post-processing DCE-MRI datasets yield significantly different values of the DCE parameters which are not interchangeable. However, high pre-treatment k_{ep} values, calculated using both models, may serve as a prognostic marker in predicting better MPM response to chemotherapy. Therefore, the use of DCE-MRI may open up the possibility for patient-tailored treatment depending on tumor biology and provide a broader prospective of the treatment effect beyond the changes in tumor thickness.

Povzetek

Izhodišča: Maligni plevralni mezoteliom (MPM) je redek in zelo agresiven maligni tumor v prsnem košu, pri večini bolnikov neozdravljiv in je povezan z izpostavljenostjo azbestu. Dinamičnokontrastno magnentoresonančno slikanje (DCE-MR) je funkcionalna slikovna metoda, ki se uporablja za oceno tumorskih mikrovaskularnih značilnosti in za sledenje učinkovitosti zdravljenja. Namen raziskave je bil primerjati dva kinetična modela, razširjeni model Tofts (ET) in adiabatični model tkivne homogenosti (AATH), za analizo DCE-MR slik in ugotoviti napovedno vrednost DCE parametrov pri zdravljenju MPM s kemoterapijo.

Metode: Prospektivna in longitudinalna raziskava je potekala v enem centru med oktobrom 2013 in julijem 2015. Bolniki so trikrat opravili DCE-MR slikanje: pred, med in po kemoterapiji. Slike smo analizirali s pomočjo ET in AATH modela. Po končani kemoterapiji smo bolnike razdelili v dve skupini, s kontrolo bolezni ali z napredovanjem bolezni, glede na modificirane kriterije za oceno odgovora solidnih tumorjev (mRECIST). Uporabili smo ROC krivuljo za ugotavljanje specifičnosti in senzitivnosti DCE parametrov za oceno tumorja na zdravljenje in teste korelacije za analizo možnosti zamenjave parametrov med modeloma.

Rezultati: V raziskavo smo vključili devetnajst bolnikov. Rezultati kažejo, da DCE parametri, ki so pridobljeni z različnimi kinetičnimi modeli, niso zamenljivi. Značilno korelacijo z odgovorom na zdravljenje smo ugotovili pri mediani vrednosti konstante refluksa (k_{ep}) pred kemoterapijo, izračunane z AATH modelom, z ocenjeno senzitivnostjo 83 % in specifičnostjo 100 % (mejna vrednost $\geq$ 0,13 /min, površina pod krivuljo 0,9). Maksimalne vrednosti k_{ep} pred kemoterapijo, izračunane z ET modelom, so nakazovale odgovor po zdravljenju, medtem ko so imele vrednosti pridobljene med zdravljenjem 100 % senzitivnost in specifičnost (mejna vrednost $\geq$0,89, površina pod krivuljo 1).

Zaključki: Rezultati raziskave kažejo, da pri uporabi ET in AATH modelov za postprocesiranje MR slik, dobimo značilno različne vrednosti DCE parametrov, ki niso zamenljive med modeloma. Kljub temu bi lahko visoke vrednosti k_{ep} parametra, izračunanega z obema modeloma, uporabili kot napovedni označevalec za boljši odgovora MPM na zdravljenje. Uporaba DCE-MRI bi lahko odprla možnosti za bolniku prilagojeno zdravljenje, odvisno od biologije tumorja, in omogočila širši pristop k oceni učinkov zdravljenja, ki presega zgolj spremembe v debelini tumorja.

Contents

List of Figures

List of Tables

Abbreviations

3D	...	three-dimensional
ADC	...	apparent diffusion coefficient
AIF	...	arterial input function
Amp	...	distribution volume of the contrast agent in the tissue of interest
AUC	...	area under the concentration curve
AATH	...	adiabatic approximation tissue homogeneity
CA	...	contrast agent
c_a	...	concentration at the arterial inlet
C_{Gd}	...	gadolinium concentration
c_v	...	concentration at the venous outflow
C(t)	...	tracer concentration in the tissue
CR	...	complete response
CT	...	computer tomography
CTC	...	common toxicity criteria
DC	...	disease control
DCE	...	dynamic contrast enhanced
DCE-CT	...	dynamic contrast-enhanced CT
DCE-MRI	...	dynamic contrast-enhanced MRI
DTPA	...	diethylene triaminepentaacetic acid
DWI	...	diffusion-weighted imaging
E	...	extraction fraction
EES	...	extravascular extracellular space
ET	...	extended Toft
F_p	...	blood volume flow rate
Gd	...	gadolinium
Hct	...	haematocrit
IVPS	...	intravascular plasma space
k_{ep}	...	flow rate constant between interstitium and plasma
K^{trans}	...	volume transfer constant
M	...	metastasis
MPM	...	malignant pleural mesothelioma
MR	...	magnetic resonance
mRECIST	...	modified response evaluation criteria in solid tumors
MTT	...	mean transit time
N	...	nodules

PET/CT	...	positron emission tomography/computer tomography
PD	...	progressive disease
PR	...	partial response
PS	...	permeability surface area product
r1	...	relaxivity constant of the contrast agent
R	...	relaxation rate
ROC	...	receiver-operating characteristics
ROI	...	region of interest
R(t)	...	residue function of the system
Sb	...	baseline/pre-contrast signal intensity
SD	...	stabile disease
S_0	...	equilibrium signal intensity
S(t)	...	tissue signal intensity
SUV	...	standard uptake value
T	...	tumor
T_1	...	relaxation time
T_{1_0}	...	intrinsic longitudinal relaxation time
T1-WI	...	T1-weighted images
T_C	...	capillary transit time
T_e	...	interstitial transit time
T_p	...	plasma mean transit time
V	...	volume of the distribution of the tracer
v_c	...	volume of intracellular space of tissue
v_e	...	interstitial volume
VOI	...	volume of interest
v_p	...	plasma volume
v_t	...	volume of the tissue
WHO	...	World Health Organization

Symbols

$\otimes$ . . . convolution operator
δ . . . dirac delta function
θ . . . flip angle
τ . . . time of injection

Chapter 1

Introduction

1.1 Asbestos

The word asbestos (meaning "unquenchable" in Greek) is a common name for a group of naturally occurring mineral silicates of the serpentine and amphibole group. Because of their tensile strength and resilient structural and chemical properties, asbestos fibres have been used in various construction and insulating purposes (Mason, Broaddus, Martin, King, & Schraufnagel, 2010).

The commercial use of asbestos started in the 19th century and grew exponentially between the two World Wars. Pathologist Dr. Cooke was the first to recognize the effects of ill health due to the inhalation of asbestos in 1924 (Cooke, 1924). The studies performed in South Africa in 1960 by Wagner and co-workers confirmed the association of asbestos with malignant disease. The country had been mining asbestos since the end of the 19th century. Several other international studies have confirmed the link between asbestos and malignant mesothelioma (Roe & Stella, 2015; van Zandwijk et al., 2013).

When the effects of ill health started to became a matter of increased public concern, the production of asbestos began to decline in Europe and North America in the late 1980s (Mason et al., 2010; Robinson & Lake, 2005). The Slovenian government has banned the manufacture, use and transport of asbestos-cement products in Slovenia with the adoption of the Asbestos Act (Zakon o prepovedi proizvodnje in prometa z azbestnimi izdelki ter o zagotovitvi sredstev za prestrukturiranje azbestne proizvodnje v neazbestno Ur.l. RS, št. 56/1996).

Almost everyone living in the western world can remember being exposed to asbestos. The exposure was primarily occupational (carpenters, plumbers, home renovators, military personnel, miners, drivers, etc.), but it can also be domestic in the households of asbestos workers or environmental. The media have given a lot of attention to asbestosis and mesothelioma because of the complex medical-legal aspect of the disease (Mason et al., 2010).

1.2 Pathogenesis of Asbestos

Asbestos causes slowly progressing fibrous processes in the lung tissue and a malignant transformation of the mesothelial cells lining of the serous cavities. Carcinogenesis induced by asbestos exposure is not yet fully understood and few plausible explanations have been proposed: mechanical irritation of pleura causing repetitive cycles of inflammation and regeneration with the consequent malignant alteration; interference into the cell mitotic process, DNA damage, induction of cytokines and growth factors, and multiple genetic changes (Mason et al., 2010).

1.3 Asbestos-Related Disease

Asbestos in exposed individuals can cause pleuro-pulmonary and extra-pulmonary benign and malign diseases (Akira, 2008).

Benign asbestos-related disease of the lung and pleura includes asbestosis, pleural plaques, rounded atelectasis and benign asbestos-related pleural effusions. The malignant disease is lung cancer and malignant mesothelioma (Akira, 2008).

In 1977, the International agency for Research in Cancer classified asbestos as a human carcinogen with the target sites being the lung, larynx and pleura. No safe lower threshold level for asbestos exposure has been identified (Roe & Stella, 2015). Cigarette smoking has proven to have a synergistic effect causing a threefold greater risk of lung carcinoma in individuals who have been exposed to asbestos (Mason et al., 2010).

Malignant mesothelioma occurs after the malignant transformation of the mesothelial cells that line the serous cavities. Predominantly it is formed on the pleura (90%), less often on the peritoneum (4-7%) and also with a very low incidence on the pericardium and tunica vaginalis testis (1%). A history of asbestos exposure is reported in 70-80% of all cases of mesothelioma (ESMO Guidelines Working Group & Manegold, 2007; Ruffie et al., 1989; van Zandwijk et al., 2013).

1.4 Malignant Pleural Mesothelioma

1.4.1 Incidence and diagnosis

Malignant pleural mesothelioma (MPM) accounts for less than 5% of all malignancies. Asbestos is the main etiological agent of malignant pleural mesothelioma (MPM). The latency period between the asbestos exposure and the development of MPM is typically long. Other recognized potential risk factors are endemic eronite exposure (seen only in Cappadocia, Turkey), therapeutic radiation and simian viruses 40. Three distinctive histological subtypes can be distinguished: epithelial, sarcomatoid and mixed or bifasic (Robinson & Lake, 2005).

Based on World Health Organization (WHO) reports, mesothelioma rates show large differences in sex and country. Male rates are much higher than female rates in virtually all countries. The sporadic background rate is around 1/1,000,000, whereas industrialized countries have a much higher rate up to 40/1,000,000 (Robinson & Lake, 2005; Scherpereel, Astoul, Baas, Berghmans, Clayson, de Vuyst, Dienemann, Galateau-Salle, Hennequin, Hillerdal, Le Pechoux et al., 2010). Its incidence in Europe is currently estimated at 20/1,000,000 (Robinson & Lake, 2005; Scherpereel et al., 2010). Based on the WHO, the global estimate of asbestos-related disease is 107,000 annual deaths (van Zandwijk et al., 2013). In Slovenia, the mean incidence in the last decade was 24/1,000,000 (Zadnik V, Primic Žakelj M. SLORA: Slovenija in rak. Epidemiologija in register raka. Onkološki inštitut ljubljana. Web site http://www.slora.si. Published December 2014. Accessed July 9, 2015.).

Patients most commonly present symptoms of dyspnea, often due to a large pleural effusion. Accompanying symptoms may be chest pain, weight loss, malaise and fatigue (Robinson & Lake, 2005).

High concentrations of serum mesothelin-related peptide were reported in mesothelioma patients. The use of serum mesothelin-related peptide as a potential tumor marker for malignant mesothelioma is promising at the time of diagnosis and for disease monitoring (Franko, Dolzan, Kovac, Arneric, & Dodic-Fikfak, 2012).

Recently, several clinical guidelines have been published on MPM (ESMO Guidelines Working Group & Manegold, 2007; Scherpereel et al., 2010; Stahel, Weder, Felip, & ESMO Guidelines Working Group, 2008; van Zandwijk et al., 2013). Often a cytology from a pleural effusion is the first diagnostic procedure to be performed, even though the accuracy of the method is low. The most reliable method for diagnosing MPM is histological sampling and immunohistochemistry that can be taken using video-assisted thoracoscopy or direct thoracoscopy (ESMO Guidelines Working Group & Manegold, 2007; Scherpereel et al., 2010; Stahel et al., 2008; van Zandwijk et al., 2013). Asbestos causes a malignant transformation of the mesothelial cells lining of the serous cavities.

1.4.2 Imaging methods and staging

Imaging plays an important role in the evaluation and staging of MPM. The disease originates in the pleural mesothelial cells and progresses locally along the pleura and fissure spaces until it encases the lungs and mediastinum. Computer tomography (CT) is currently the primary imaging modality for the diagnosis and evaluation of MPM, showing MPM as an encircled rind of the tumor or an extensive lobulated pleural-based tumor mass, with a thickened interlobar fissure and/or enlarged mediastinal lymph nodes, often a pleural effusion and volume reduction of the chest (Wang et al., 2004).

Thoracic magnetic resonance imaging (MRI) is used as a complementary imaging method to CT. The advantages of MR morphological imaging are better soft tissue contrast with no use of ionization radiation. It is superior to CT in identifying a local invasion by mesothelioma into the diaphragm (CT accuracy 55%, MR 82%, $P = 0.01$), the endothoracic fascia or solitary foci of a chest wall invasion (CT accuracy 46%, MR 69%, $P = 0.05$) (Entwisle, 2004; Wang et al., 2004; Zahid, Sharif, Routledge, & Scarci, 2011). MPM has an intermediate to slightly high signal intensity on T1-weighted images (T1-WI) and a moderately high signal intensity on T2-weighted images (T2-WI) as compared to adjacent chest wall musculature and shows moderate enhancement after the administration of a gadolinium contrast agent (Gill et al., 2010; Podobnik, Kocijancic, Kovac, & Sersa, 2010). Artefacts are common in thoracic MRI due to the respiratory and cardiac motion, which can be solved with consecutive breath-hold technique and with the use of respiratory cycle and/or cardiac gated imaging. Thoracic MR can provide morphologic but also functional information. With functional imaging we can obtain information either of the macroscopic motion (dynamic visualization of cardiac, chest wall and diaphragmatic movement) or microscopic motion (diffusion imaging). Dynamic MRI can be performed in patients who are candidates for surgery and have equivocal MPM infiltration into the heart chambers (or other thoracic structures, e.g. the chest wall, great vessels, diaphragm). Dynamic images are obtained during several respiratory and/or cardiac cycle using sequences of high temporal resolution. Slice position should be perpendicular to the interface between the MPM and the underlying thoracic structure. This allows visualization of the MPM mobility during breathing and/or cardiac cycle which is a sensitive method for assessing MPM invasion into the thoracic structures. Adequate sequences for dynamic MR studies are steady-state free procession sequences (Khalil et al., 2016). Similar imaging principles are applied when dynamic MR studies are used in body imaging for the visualisation of organ movements (Colaiacomo et al., 2009; Kulinna-Cosentini, Schima, & Cosentini, 2007; Vivoda Tomšič & Podkrajšek, 2017).

Diffusion-weighted MRI has shown a lot of potential in oncological applications. The diffusivity of water molecules is quantitatively assessed using the apparent diffusion coefficient. Until now, diffusion-weighted imaging (DWI) in MPM has been used in a study where the apparent diffusion coefficient (ADC) values were correlated with the histological type of mesothelioma showing the differences between the sarcomatoid and the epiteloid

type. Other studies used DWI to differentiate malignant from benign pleural disease (Coolen et al., 2012; Gill et al., 2010).

In positron emission tomography (PET) the positron-emitting radionuclides of several elements are used to obtain quantitative tomographic images. 18F-Fluorodeoxyglucose (FDG) PET demonstrates the metabolic activity within a tumor. It has been combined with CT to provide anatomic information. It is used in some centres as an additional imaging method in MPM for detecting metastatic lymph nodules that appear normal on the CT and MR and extra thoracic metastasis, thus increasing the accuracy in staging (ESMO Guidelines Working Group & Manegold, 2007; Scherpereel et al., 2010; Stahel et al., 2008; van Zandwijk et al., 2013).

Laparoscopy is recommended for a more precise staging in patients who are candidates for surgery and have suspicious finding on imaging study for intra-abdominal disease (Entwisle, 2004; Wang et al., 2004).

The staging of MPM is based on the TNM staging system (T-tumor, N- nodules, M-metastasis) developed in 1995 by the Mesothelioma interest Group and adopted by the International union against cancer (Rusch, 1995; Sobin, Gospodarowicz, & Wittekind, 2009).

1.4.3 Management of MPM

Management options include chemotherapy and surgical therapy. Only 5% of the patients, the ones with localized disease and in good general condition, are suitable for curative surgery (Robinson & Lake, 2005).

Chemotherapy is the standard management modality for most patients and despite all efforts, the overall survival remains poor, from 9 to 17 months (Gill et al., 2010; Saddoughi, Abdelsattar, & Blackmon, 2018). The goal is to decrease the tumor burden, relieve the symptoms and prolong the survival of the patients. A combination of chemotherapeutics has proven to be more effective and shows a superior survival of patients compared to monotherapy (Scherpereel et al., 2010). The present standard of care for first-line systemic treatment is cisplatin plus pemetrexed with median overall survival time of 12.1 months (Zalcman et al., 2016). A phase II trial of cisplatin and gemcitabine has proven to prolong the median survival time to 17 months and the time to progression to 8 months (Kovac et al., 2012).

Recent studies in radiotherapy have shown promising results for locoregional control (Armato et al., 2013). Radiotherapy is used mostly for local postsurgical radiotherapy (Robinson & Lake, 2005). Other therapies currently in clinical trials include immunotherapy, gene therapy, photodynamic therapy and new regimens of chemotherapy (Robinson & Lake, 2005).

1.4.4 Evaluation of MPM response to therapy

Current clinical therapy response validation in MPM is based on the evaluation of morphological images based on mRECIST criteria (modified Response Evaluation Criteria in Solid Tumors). Studies measuring the tumor volume by the volumetric approach were conducted, but as the technique is semi quantitative and time consuming, it did not come into everyday clinical use (Armato et al., 2013).

Chemotherapeutic agents, apart from exerting a cytostatic effect, can target other anti-cancer mechanisms such as vascular endothelium (anti-vascular therapies) or the mechanism of neoangiogenesis (anti-angiogenetic therapies). Cisplatin used in monotherapy and in doublet for the treatment of MPM has a cytotoxic and anti-angiogenic effect (Cemazar et al., 2001; Clements, Jones, Cumming, & Daoud, 1999). There is increasing

awareness that the anatomical approach based on tumor volume measurements may not be sensitive enough to measure the effect of anti-angiogenic and vascular-targeted therapeutics. Furthermore, size change due to cell death and tumor shrinkage, as a response to chemotherapy, can be manifested later than changes in tumor tissue pathophysiology such as tumor vascularization and permeability.

Dynamic contrast-enhanced CT (DCE-CT) and MRI (DCE-MRI) are both functional imaging techniques used to analyze tumor microvascular properties. DCE-CT exposes patients to considerable local radiation which limits its use in research setting. Therefore, DCE-MRI is the method of choice in research and in pre-clinical studies for the evaluation of early response to treatment (Galbraith, 2006).

1.4.4.1 mRECIST criteria

The clinical standard to measure the mesothelioma response to therapy is specific mRECIST which is the adapted approach of the RECIST criteria due to the specific growth pattern of MPM. They are done by uni-dimensional measuring the tumor thickness perpendicular to the chest wall or the mediastinum, measured at 2 sites at 3 different levels in CT or MR. The sums of 6 pleural measurements define one univariate diameter. In the baseline study, the sum represents the baseline tumor burden. During the control study, which must be at least 4 weeks apart, the tumor thickness is measured at the same level and same position. The response is assessed depending on the change in total tumor measurement and defined as a complete response, partial response, stable disease or progressive disease at reassessment (Byrne & Nowak, 2004).

Tumor response is defined as:

1. Complete response (CR) – disappearance of all known disease, determined by two observations not less than 4 weeks apart.
2. Partial response (PR) – at least a 30% reduction in the total tumor measurement on two occasions not less than 4 weeks apart.
3. Stable disease (SD) – neither fulfil the criteria for PR nor PD.
4. Progressive disease (PD) – increase of at least 20% in the total measurement or appearance of the new ones. One or more new lesions.

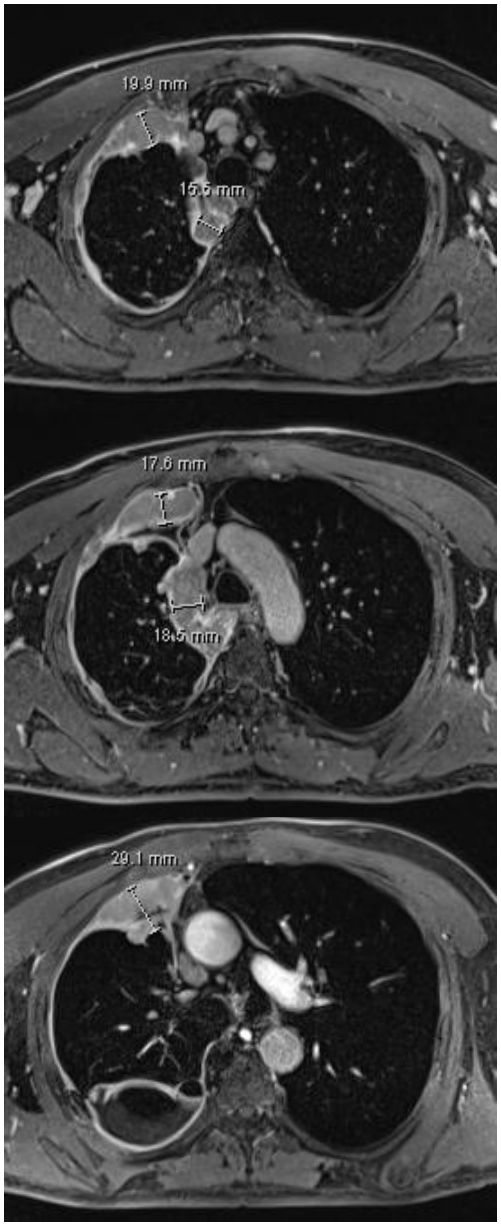

Figure 1.1: An example of the MPM measurements according to the mRECIST. Post-contrast T1-weighted fat-sat images in the axial plane of the thorax. Total measurements: 20 + 16 + 18 + 18 + 29 = 101 cm. At reassessment, it is important to perform the measurements in the same position.

1.4.4.2 Dynamic contrast-enhanced MRI

DCE-MRI is a functional imaging technique used to analyze tumor microvascular properties. It is based on the intravenous application of a contrast agent followed by the continuous acquisition of MR images over the tissue of interest at various time points in order to track a bolus of the contrast material as it enters the tissue and is subsequently washed out (Padhani & Khan, 2010).

Paramagnetic contrast agents (CA) are organic molecules with a paramagnetic nucleus. In practice only a gadolinium (Gd) based contrast agent is used. Gd is a rare earth metal more commonly known as heavy metal. It is toxic in free state and needs to be bound with chelate to form a water-soluble and relatively safe contrast agent for the MR. By binding

Gd with diethylene triaminepentaaceic acid (DTPA), Gd-DTPA is formed. Gd causes a shortening of the relaxation times of the surrounding protons. It shortens the T1 and T2 relaxation times. This results in a signal increase in the T1-WI and a signal decrease in the T2-weighted images (Westbrook.C., 2005). The T1-WI is the technique preferred after the contrast medium intravenous injection. T1-weighted DCE-MRI studies in tumors are most commonly performed using a gradient-echo sequence, as they provide a high spatial resolution and the acquisition times allow a sufficient temporal resolution for the analysis of the DCE-MRI datasets (Heilmann, Kiessling, Enderlin, & Schad, 2006; Naish et al., 2009). Gd-DTPA is the most widely available contrast agent compared to other contrast agents (large-molecular agents and agents that are retained in vascular compartments) (Galbraith, 2006). Gd-DTPA can easily diffuse from a vasculature to an interstitial space but cannot cross the cell membrane and therefore is considered as extravascular extracellular tracer (Sourbron & Buckley, 2013). The rate of diffusion of this tracer depends on a combination of tissue perfusion, vascular permeability and the capillary surface area (Westbrook.C., 2005).

Dynamic contrast enhanced imaging (DCEI) data can be analyzed by the quantitative and semi-quantitative method. For the quantitative method to be performed, the initial T1-relaxation rate of the tissue needs to be measured. The variation in the value needs to be corrected when calculating the change in the signal intensity enhancement and tracer concentration. If this is not performed, such as in the semi-quantitative method, the parameters assessed cannot be used for comparison in different patients or with different tissues, but can be used to compare changes in response to the therapy within the same tissue. The semi-quantitative method is reproducible but depends on the protocol used. The quantitative method, using tracer-kinetic modelling, allows an estimation of the parameters independent of the protocol or the equipment used and allows for the comparison in different patients, tissues and during therapy (Galbraith, 2006; Padhani & Khan, 2010).

The most commonly used two-compartment model of the DCE-MRI analysis in clinical practice is the extended Tofts (ET) model. The model allows the estimation of the volume transfer constant (K^{trans}), the plasma volume (v_{p}) and the interstitium volume (v_{e}). In this method, K^{trans} does not directly estimate perfusion as it depends on the conditions of the blood flow and capillary permeability. This model also does not calculate the time needed for a tracer to pass from an arterial to the venous side of the capillary (T_{c}). For a more accurate tissue characterization, more complex models need to be used, assessing more parameters. The adiabatic approximation tissue homogeneity (AATH) model allows the determination of addition parameters: blood volume flow rate (F_{p}), the permeability surface area product representing a flow through the vessel wall (PS), T_{c}, the flow rate constant between the EES and the plasma (k_{ep}) and the extraction constant (E) (Tofts et al., 1999).

Two studies have been published using DCE-MRI in MPM. Coolen and co-workers used DCE-MRI to improve the accuracy of the diagnosis of MPM with MR, while Giesel and co-workers proved that changes in the quantitative parameters of DCEI were predictive of therapy response (Coolen et al., 2012; Giesel et al., 2006). To the best of our knowledge, no study has been conducted to identify which model of the DCEI analysis best assesses the change in MPM pathophysiology and vasculature during the course of therapy.

Chapter 2

Aims and Hypothesis

The purpose of this study is to examine the different models of DCEI analysis. We compared the extended Tofts model with a more complex adiabatic approximation tissue homogeneity model.

The goal is to identify the perfusion model that best describes the changes in MPM tissue pathophysiology during the course of therapy.

The reference for the evaluation were the tumor's morphological measurements during the course of the therapy, according to the mRECIST.

Our hypotheses were:

I. There are significant changes in the values of the perfusion parameters prior to therapy, during the therapy and post-treatment.
II. The changes in the measured perfusion parameters do not differ significantly between the models.
III. The changes in perfusion parameters during the course of the therapy reflect the changes defined by the RECIST criteria.
IV. DCE changes may serve as significant predictors for the response to therapy.

Chapter 3

Materials and Methods

3.1 Patient Selection

This was a prospective study acquiring data from October 2013 until July 2015. All patients with biopsy-proven malignant pleural mesothelioma eligible for chemotherapy and treated at our institution were recruited. Inclusion criteria for the study were the following: all patients have to be older than 18 years of age, have histologically proven malignant pleural mesothelioma and Karnofsky performance status ≥60% or Eastern Cooperation Oncology Group performance status between 0 and 2. Exclusion criteria were as follows: other malignant disease (excluding in situ cervical cancer and non-melanocytic skin cancer), acute infection, inadequate hematopoietic function (haemoglobin < 100 g/L, neutrophils < 1x10^9/L, platelets < 100 x 10^9/L), decompensated heart failure, inadequate liver function (bilirubin > 1.25 x upper normal limit, AST/ALT > 2 x upper normal limit), chronic kidney disease (glomerular filtration rate < 60 mL/min/1.73 m2), peripheral sensory neuropathy grade ≥ 2 according to Common Toxicity Criteria (CTC), vascular disorder grade ≥ 2 according to CTC, positive pregnancy test, absolute or relative contraindication to magnetic resonance imaging and gadolinium administration. The study was approved by the local ethics committee and all patients gave informed consent for participating in the study. Each patient was examined 3 times during chemotherapy with MR, including DCE-MRI: before the start of the chemotherapy, after finishing the third cycle and at the end of chemotherapy.

3.2 Treatment Schedule

The treatment schema included gemcitabine at a dose of 250 mg/m2 in a 6-hour infusion on days 1 and 8, and cisplatin at 75 mg/m2 on day 2 of a 3-week cycle. After 4 cycles, patients received 2 cycles of monotherapy with gemcitabine at 250 mg/m2 in prolonged infusion on day 1 and 8 (Kovac et al., 2012). Patients with poor performance status received a 3-week cycle with low-dose gemcitabine in long infusion 200 mg/m2 over 6h on day 1 and cisplatin at 60 mg/m2 on day 2 (Zwitter, Kovac, Rajer, Vrankar, & Smrdel, 2010). Some patients received pemetrexed at 500 mg/m2 and cisplatin at 75 mg/m2 (Vogelzang et al., 2003).

3.3 MR Imaging Protocol

The MR thoracic studies were performed by using the 3 Tesla magnetic resonance system (Trio, Siemens Healthcare, Erlangen, Germany) with 6-channel body matrix coil and phase

array spine matrix coil in supine position. The study started by obtaining anatomic images: T2-weighted turbo spin echo sequence with fat saturation in axial plane covering the whole thorax from clavicles to diaphragm using the following parameters: repetition time [msec]/echo time [msec] 3000/99, 24 sections with an 8-mm section thickness, 1.6 mm gap, 340x250 mm field of view, 189x320 matrix, yielding a voxel resolution of 1.3 x 1.1 x 8 mm, respiratory triggered; T1-weighted tree-dimensional (3D) gradient-echo breath hold sequence (VIBE) with the following parameters: repetition time [msec]/echo time [msec], 3.18/1.15, 346x324 mm field of view, 1.3 x 1.1 x 1.5 mm voxel size, 246 x 320 matrix, 96 slices, 1.5 mm slice thickness, 0:39 minute imaging time. DCE-MRI scans were performed over part of the thorax showing tumor burden using a T1-weighted 3D gradient echo sequence (turbo-FLASH) with the following parameters: repetition time [msec]/echo time [msec], 4.5/1.16, flip angle 15°, 330x330 mm field of view, 192x192 matrix, 1.7x1.7x5 mm voxel size, 30 slices per slab with a 5 mm section thickness, with a temporal resolution of 18 seconds per scan. Gadolinium CA (Gadovist, Gadobutrol, Berlin, Germany) was administered through the intravenous catheter after the third repetition at a dose of 0.1 mmol/kg followed by 30 ml of saline flush, both at the rate of 3.5 ml/s using a power injector (Medrad, Spectris Solaris EP). Images were acquired during shallow breathing, a total of 20 sequential repetitions were acquired for 5:58 minutes. Prior to the dynamic image acquisition, pre-contrast T1-WI were acquired with 2 averages and flip angles of 2°, 10° and 15° for T1 mapping. The study proceeded with obtaining 3D gradient-echo breath-hold post-contrast T1-weighted images with the same parameters as the previous non-enhanced T1-weighted images.

3.4 Imaging Data Analysis and Processing

All conventional and DCE-MR images were consensually analyzed by the same two radiologists with 5 and 15 years of experience respectively in thoracic radiology. Tumor TNM stage was determined according to the 7th edition of the TNM classification for MPM (Sobin et al., 2009). DCE-MRI source data were post-processed on a separate workstation using commercially available software (Olea Medical 2.3, La Ciotat, France). Motion correction and signal smoothening was performed. Regions of interest (ROI) were drawn freehand around the MPM periphery in each section avoiding large vessels, readily recognizable necrotic tissue (low-attenuation nonenhancing areas within tumors), adjacent atelectasis and surrounding normal tissue.

3.4.1 Contrast agent concentration calculation

The CA concentration calculation was based on an assumed linear relationship between CA concentration and the longitudinal relaxation rate:

$$\frac{1}{T_1(t)} = \frac{1}{T_{1_0}} + r_1 \cdot C(t) \tag{3.1}$$

where r_1 is the spin-lattice relaxivity constant of the CA and T_{1_0} is intrinsic longitudinal relaxation time in the absence of the CA. Inverse relaxation time is known as relaxation rate R. Equation 3.1 can be expressed as:

$$\Delta R_1(t) = R_1(t) - R_{1_0} = r_1 \cdot C(t) \tag{3.2}$$

where R_{1_0} is relaxation rate in the absence of CA.

The T_{1_0} was determined based on the non-linear equation for signal of the gradient-echo sequence with termination of the residual transverse magnetization (Heilmann et al., 2006)

using three sets of gradient echo images with different flip angles. The respective signal is modelled as

$$S(\theta) = S_0 \sin\theta \frac{1 - \exp(-\frac{TR}{T_1})}{1 - \cos\theta \exp(-\frac{TR}{T_1})} e^{-\frac{TE}{T2}^*}, \tag{3.3}$$

where S_0 is the signal intensity from the excited sample volume that would follow immediately after the 90° excitation pulse, while θ is the actual excitation flip angle. With this technique we obtained a map of T_{1_0} values for the image slab also known as a T_1 map. The signal dependence on T_2* can be neglected since TE << T_2*. This yields the following formula for the pre-contrast/baseline signal intensity (Sb):

$$Sb = S_0 \sin\theta B \tag{3.4}$$

where

$$B = \frac{1 - \exp(-\frac{TR}{T_{1_0}})}{1 - \cos\theta \exp(-\frac{TR}{T_{1_0}})} \tag{3.5}$$

With the inflow of CA in the tissue, T_1 relaxation rate changes, causing the change in the tissue signal intensity $S(t)$, which can be expressed by the equation

$$S(t) = S_0 \sin\theta \frac{1 - \exp(-\frac{TR}{T1(t)})}{1 - \cos\theta \exp(-\frac{TR}{T1(t)})}. \tag{3.6}$$

By dividing the result of Eq. 3.6 with Eq. 3.4 1/ T_1 (t) can be isolated, which leads to

$$\frac{1}{T_1(t)} = \frac{-1}{TR} ln\left[\frac{1 - \frac{S(t)}{Sb} B}{1 - \cos\theta \frac{S(t)}{Sb} B}\right]. \tag{3.7}$$

The result of Eq. 3.7 can then be used for substitution in Eq. 3.2, yielding the equation that relates the dynamic signal intensity to the contrast agent concentration,

$$\Delta R_1(t) = \frac{-1}{TR} ln\left[\frac{1 - \frac{S(t)}{Sb} B}{1 - \cos\theta \frac{S(t)}{Sb} B}\right] - \frac{1}{T_{10}}. \tag{3.8}$$

Spin-lattice relaxivity constant of the CA was r_1 = 3.8 s^{-1} mM^{-1} (at 37°C) for gadolinium chelate at the 3T magnetic field strength (Shen et al., 2015) and C is the Gd chelate concentration (mmol/L).

3.4.2 Arterial input function

For each slice in the image volume 20 dynamic scans are averaged; this resulted in a high signal to noise ratio data set representing the average intensity over time for each voxel from which it is straightforward to locate the aorta. After manually selecting the aorta, the evolution of the signal of each pixel during the dynamic acquisition was allowed to obtain the concentration curve in the aorta or arterial input function (AIF). An example of AIF is shown in Figure 3.1.

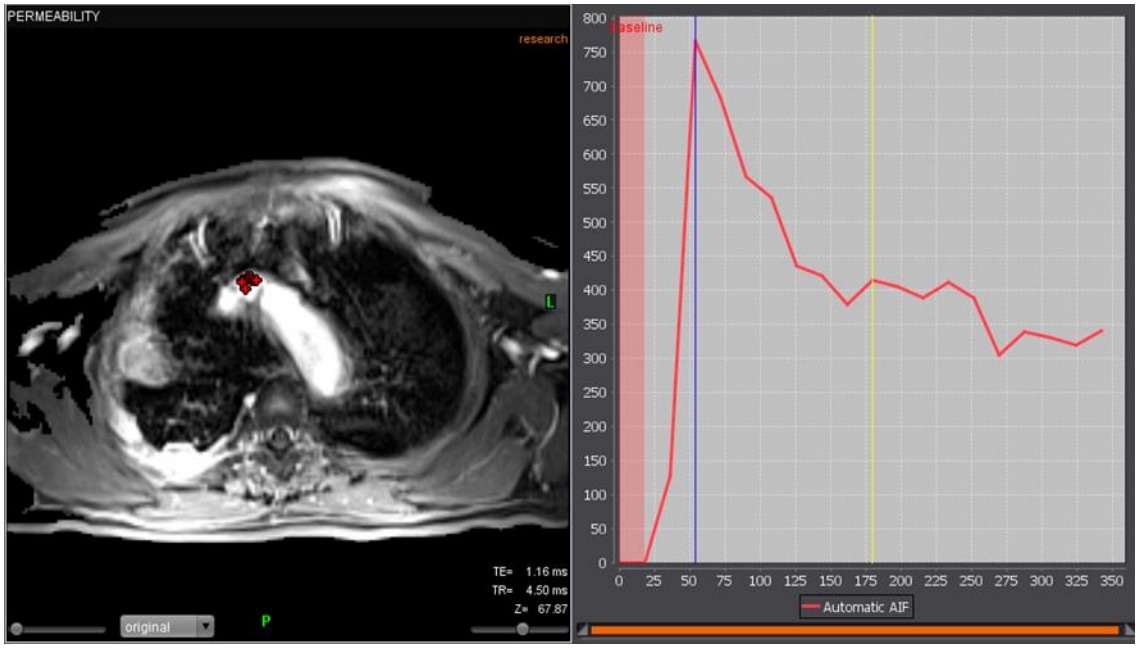

Figure 3.1: Arterial input function curve. a) Post-contrast T1-weighted fat-sat images in the axial plane of the thorax. Red dots indicate the location of the aorta. b) Arterial input function curve obtained in the aorta has an early rise, sharp peak, and captures a late plateau consistent with the physiological blood circulation in the large vessels. The AIF corresponds to the plasmatic concentration at the arterial inlet (c_a) of the capillary when corrected for the existence of blood cells. We used the standard value of haematocrit of 0.45 corresponding to the value in the major blood vessels (Fan et al., 2010).

$$c_a(t) = \frac{AIF}{1 - Hct} \tag{3.9}$$

3.4.3 Tracer kinetic analysis

A capillary-tissue system was used to model the vasculature within the volume of interest on the DCE-MRI as schematically represented in Figure 3.2.

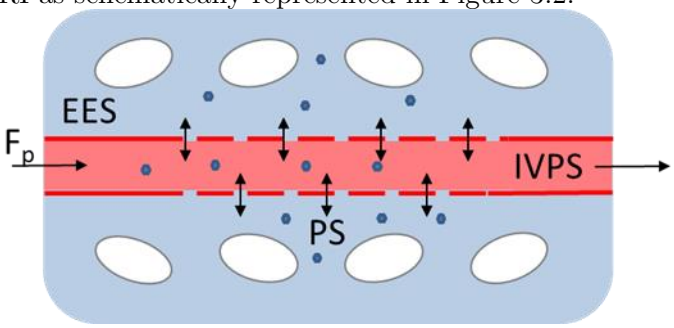

Figure 3.2: Architecture of the capillary-tissue system. It is composed of the capillary or intravascular plasma space (IVPS) (red), the interstitium or extravascular extracellular (EES) (blue) and intracellular space (white). The CA (dark blue dots) or tracer enters the plasma space via the blood flow Fp, it is then distributed in the IVPS and is bidirectionally exchanged between the IVPS and EES as shown with black arrows and expressed by the permeability-surface area product PS. The CA cannot enter the cells (white). In the tracer kinetic modelling, this exchange model is called a two-compartment model, composed of a plasmatic and an interstitium compartment.

The tissue concentration C(t) (in M) is the number of CA or tracer molecules in the tissue relative to the total volume of tissue. C(t) is a directly measurable quantity. The tracers volume of distribution v is the fraction of tissue that is accessible to the tracer molecules (dimensionless or in ml/100 ml). The tracer concentration c(t) within the distribution space (in M) is defined as the number of tracer molecules relative to the volume of distribution c.

$$c(t) = \frac{C(t)}{v} \tag{3.10}$$

A sum of all tissue volume fractions (of the various spaces) must meet the following condition:

$$v_p + v_e + v_c = 1 \tag{3.11}$$

where v_p, v_e, and v_c represent fractional volumes of IVPS, EES and intracellular space respectively. The total tracer concentration $C(t)$ at a given time point t is:

$$C(t) = v_p c_p(t) + v_e c_e(t) \tag{3.12}$$

where c_p and c_e are tracer concentrations in the IVPS and EES, respectively.
The tracer enters the capillary bed through the arterial inlet “a”, then travels by and exits through the venous outlet “v”. The input of the system is the arterial inflow c_a(t) or the arterial input function and the output is the venous outflow c_v (t) as schematically represented in Figure 3.3.

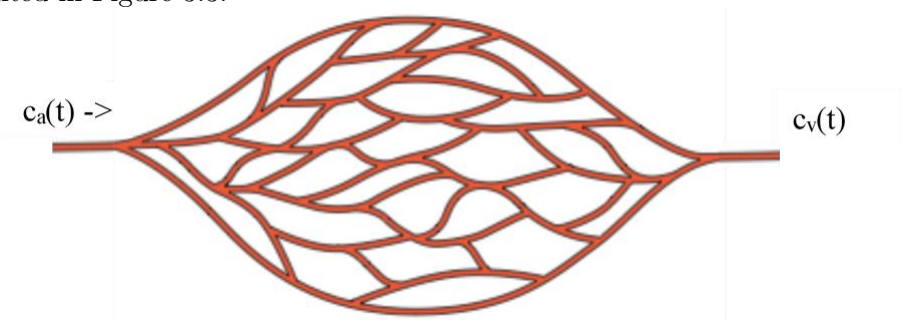

Figure 3.3: Architecture of the capillary bed. The tracer enters the capillary bed (red) at the arterial inlet and exits through the venous outlet. The input is denoted as arterial inflow c_a(t) or arterial input function and the output is the venous outflow c_v (t) ("Perfusion model".2013).

The most general principle in tracer-kinetic theory is the conservation of tracer mass, which can be rewritten as:

$$\frac{dC(t)}{dt} = F_p[c_a(t) - c_v(t)] \tag{3.13}$$

The blood flow (F_p) is defined as the volume flow rate of the blood through the vascular compartment in the 100 ml of tissue and has the unit of ml/min/100 ml.
Between the c_v(t) and c_a(t) exists an impulse response function $h(t)$ that can be expressed as a convolution product:

$$c_v(t) = c_a(t) \otimes h(t) \tag{3.14}$$

where $\otimes$ is the convolution operator. As both functions, arterial inflow and impulse response, are zero for negative times, the convolution operator in Eq. 3.14 is equal to:

$$c_a(t) \otimes h(t) = \int_0^t dt' \; c_a(t') \; h(t - t') \tag{3.15}$$

The transport of the tracer in the tissue is characterized by a probability distribution of transit times $h(t)$ (min^{-1}) or system input response. The first momentum the impulse response $h(t)$ is known as a mean transit time (MTT) of the system, i.e. the average time that the CA remains in the tissue.

$$MTT = \int_0^\infty t \; h(t) \; dt \tag{3.16}$$

The relation in Eq. 3.14 can be inserted in Eq. 3.13 which yields:

$$\frac{dC(t)}{dt} = \; F_p[c_a(t) - c_a(t) \otimes h(t)] \tag{3.17}$$

Arterial inflow function can be expressed also by a convolution of it with Dirac's delta function δ(t) which preserves the input function:

$$c_a(t) \otimes \delta(t) = \int_0^t dt' \; c_a(t') \; \delta(t - t') = \; c_a(t) \tag{3.18}$$

This relation can then be inserted in Eq. 3.17, obtaining

$$\frac{dC(t)}{dt} = \; F_p c_a(t) \otimes [\delta(t) - h(t)] \tag{3.19}$$

In the next step this function is integrated over time in the interval from 0 to t which yields:

$$\begin{aligned} C(t) = \int_0^t \frac{dc}{dt'} dt' = \; \int_0^t dt' \left[F_p c_a(t') \otimes [\delta(t') - h(t')] \right] = \\ = F_p \int_0^t dt' \int_0^{t'} dt'' c_a(t'') \; [\delta(t' - t'') - h(t' - t'')] = \\ = F_p \int_0^{t'} dt'' c_a(t'') \int_0^t dt' \; [\delta(t' - t'') - h(t' - t'')] = \\ = F_p \; c_a(t) \otimes \left[1 - \int_0^t dt' \; h(t') \right]. \end{aligned} \tag{3.20}$$

Here, the relation $\int_0^t dt' \delta(t' - t'') = 1$ for $0 < t'' < t$ was used. Equation 20 can be rewritten as the perfusion model formula:

$$C(t) = F_p c_a(t) \otimes R(t) \tag{3.21}$$

R(t) is the residue function of the system. It can be expressed by the formula:

$$R(t) = 1 - \int_0^t h(t')dt' \tag{3.22}$$

$R(t)$ represents the fraction of the CA (tracer molecules) that remains in the tissue at time t. The tracer mean transit time MTT can also be expressed as

$$MTT = \int_0^\infty R(t)dt \tag{3.23}$$

The perfusion equation can also be modified by taking into account the delay of the arrival of the contrast agent τ within the tissue in respect to the measurement of the AIF in the large vessel:

$$C(t) = F_p c_a(t - \tau) \otimes R(t) \tag{3.24}$$

The capillary-tissue system is modelled as linear and stationary. We make two assumptions regarding the tissues' residue response $R(t)$: i) we assume that R is proportional to the injected tracer concentration c and by that we pertain to the linearity of the system, ii) we further assume that the transit-time distribution does not depend on the time of injection τ and thus refer to the stationary system (Koh, Bisdas, Koh, & Thng, 2011; Sourbron & Buckley, 2013).

Given the tracer tissue concentration C(t) and the concentration in the blood plasma of the feeding artery c_a(t), the F_p and R can be deduced by the process called deconvolution. Deconvolution can be done by model-fitting approach to extract information from the tissue, such as the volume of the individual space and the exchange rates between them. We have analysed our data using the extended Tofts model and the adiabatic approximation tissue homogeneity model also known as the Lawrence and Lee model. The main model parameters are (i) volume and flow parameters, (ii) mean transit times, (iii) extraction fraction, and (iv) transfer constants as presented in Table 3.1.

Table 3.1: List of the main model parameters describing the tissue.

Symbol	Interpretation	Unit
Volume and flow parameters		
v_e	interstitial volume	ml/100ml
v_p	plasma volume	ml/100ml
PS	permeability-surface area product	ml/min/100ml
F_p	blood volume flow rate	ml/min/100 ml
Mean transit time		
MTT	mean transit time	min
T_e	interstitial transit time	min
T_p	plasma mean transit time	min
T_c	capillary transit time	min
Extraction fraction		
E	extraction fraction	%
Transfer constants		
K^{trans}	volume transfer constant	1/min
k_{ep}	rate constant between the interstitium and plasma	1/min

3.4.3.1 Extended Tofts model

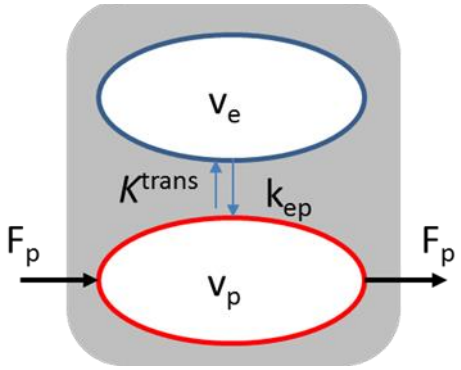

Figure 3.4: The architecture of the extended Tofts model. The tissue (grey) contains the plasma space (red, lower) and EES (blue, upper). The tracer is at a constant flow F_p into the plasma space v_p. The tracer leaks from the plasmatic space into the interstitial space at the rate of K^{trans} and returns at the rate of k_{ep}.

The extended Tofts model is a conventional two-compartment model, where both the plasma and interstitial space are modelled as well-mixed compartments. The tracer concentration in the plasma is uniform through the capillary system. The mass balance for the model is given by the equation:

$$C(t) = v_p c_p(t) + v_e c_e(t) = v_p c_p(t) + K^{trans} c_p(t) \otimes exp(-k_{ep} t) \tag{3.25}$$

K^{trans} denotes the volume transfer constant (1/min) from the plasmatic space into the interstitial space.

$$K^{trans} = \frac{F_p PS}{F_p + PS} \tag{3.26}$$

K^{trans} is a product of the blood volume flow rate F_p and the permeability-surface area product PS. It is defined as an outflow of the tracer per unit of time, tissue volume and tissue plasma concentration. K^{trans} and F_p cannot be separately measured in the extended Tofts model, thus the physiological interpretation of K^{trans} depends on the transport conditions. In the fast tracer exchange condition PS is much larger than F_p so that $K^{trans} = F_p$ or the delivery of the tracer is flow-limited. The other extreme is slow tracer exchange regime where PS is much smaller than F_p. In that case $K^{trans} = PS$ or the delivery is permeability limited. If the tissue conditions are flow and permeability limited, K^{trans} is mainly determined by the smaller of the two. k_{ep} denotes the efflux (backflux) rate between the interstitium and the plasma:

$$k_{ep} = \frac{K^{trans}}{v_e} \tag{3.27}$$

The impulse residue function R is modelled by an exponentially decaying function:

$$R(t) = Ee^{-k_{ep}\, t} \tag{3.28}$$

Where E is the extraction fraction (%), defined as the fraction of the tracer that is extracted into the interstitium and is given by:

$$E = \frac{PS}{PS + F_p} \tag{3.29}$$

3.4.3.2 Adiabatic approximation tissue homogeneity model or Lawrence and Lee model

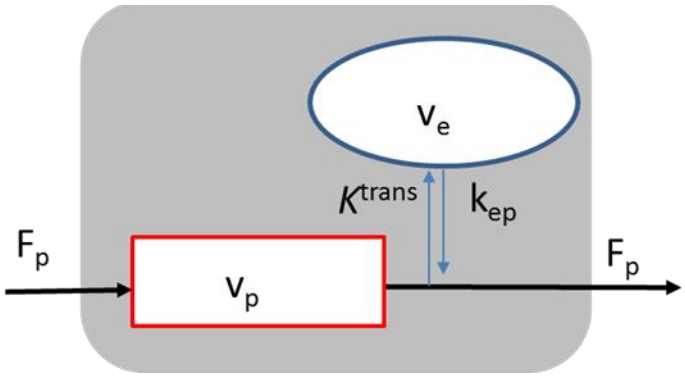

Figure 3.5: The architecture of the AATH model. The tissue (grey) contains the plasma space (red, lower) and EES (blue, upper). The tracer is at a constant flow F_p into the plasma space v_p. When reaching the venous end of the capillary (PS=0), the tracer leaks to the interstitial space at the rate of K^{trans} and returns at the rate of k_{ep}.

The adiabatic approximation tissue homogeneity model (AATH) is a two-compartment model where the capillary tracer's concentration is dependent on time and distance in the capillary. The EES is a well-mixed compartment. The tracer exchange takes place at the venous end of the capillary. The term adiabatic refers to a situation where the tracer concentration changes more slowly in the EES than in plasma. The mass conservation for the interstitium and plasma can be expressed as

$$v_e \frac{dc_e}{dt}(t) = K^{trans} c_p(L,t) - K^{trans} c_e(t), \tag{3.30}$$

$$v_p \frac{\partial c_p}{\partial t}(x,t) = -F_p L \frac{\partial c_p}{\partial x}(x,t), \tag{3.31}$$

where L is the tube length and x is the position along the tube, $x = 0$ at the arterial inlet and $x = L$ at the venous outlet. With the boundary conditions $c_p(x,0)$ and $c_p(0,t)=0$, the solution is:

$$c_p(x,t) = c_a(t - \frac{v_p}{F_p}\frac{x}{L}) \tag{3.32}$$

With the mass balance formula form the model is:

$$C(t) = F_p c_p(t) \otimes R(t) \tag{3.33}$$

The capillary transit time T_c is given by the formula:

$$T_c = \frac{v_c}{F_p} \tag{3.34}$$

The impulse residue function depends on the transport phase of the tracer. In the vascular phase ($0 < t < T_c$), the vascular space is considered impermeable and R equals 1. In the parenchymal phase ($t > T_c$), the R function is expressed as:

$$R(t) = \begin{cases} 1 & t \leq T_c \\ E \exp\left(\frac{-F_p E}{v_e}(t - T_c)\right) & t > T_c \end{cases} \tag{3.35}$$

3.5 Evaluation of Response

Tumor response to therapy was assessed by the same two radiologists using MR images at the intra-treatment and post-treatment study according to modified Response Evaluation Criteria in Solid Tumors (mRECIST) (Byrne & Nowak, 2004). Patients demonstrating stable disease and partial response were classified as having disease control (DC) and patients with progressive disease as having progressive disease (PD).

3.6 Statistical Analysis

The Shapiro-Wilk test was used to test for the normal distribution of the data. If the perfusion values in the population were normally distributed, parametric methods were applied. Otherwise, non-parametric paired samples test was selected for the statistical analysis.

The paired samples t test was applied to detect any statistically significant difference on the obtained DCE parameter values using both models and any difference between DCE parameters in each model.

Bland-Altman plot analysis was used to explore whether DCE parameters during the course of chemotherapy could be interchangeable between the models.

Independent samples t test was used to detect if changes in DCE parameters during the course of the therapy reflect the changes defined by the mRECIST criteria between the group of patients with DC and PD.

Receiver-operating characteristics (ROC) curve was used to examine specificity and sensibility of DCE parameters for predicting response to therapy.

The results were considered significant if P value $< .05$. P values were adjusted for multiple testing (Bonferroni correction).

The results were analyzed and graphs performed using MedCalc Statistical Software version 15.6.1 (MedCalc Software bvba, Ostend, Belgium; https://www.medcalc.org).

Chapter 4

Results

Twenty-nine consecutive patients were recruited in the trial. Six patients died before the end of the chemotherapy, 2 suffered a major vascular event and discontinued the chemotherapy, 1 suffered from claustrophobia and refused further participation in the study and 1 underwent lobectomy with pleurectomy after the third cycle of chemotherapy.

Nineteen patients (16 men and 3 women, median age 68 years, range 46-84) formed the study population. Patient demographic and clinical data are shown in Table 4.1. Each patient was examined 3 times during chemotherapy with MR, including DCE-MRI: 1) at the pre-treatment study (median time interval 4 days, range 7–0 days), 2) at the intra-treatment study after finishing the third cycle (median time interval 8 days, range 7–14 days), and 3) at the post-treatment study after finishing the sixth cycle chemotherapy (median time interval 12 days, range 7 to 14 days). Six patients were classified as having PD and 13 as DC.

Table 4.1: Demographic and clinical data.

Patient	Sex/Age, years	Histology	Cycle of chemotherapy	Asbestos exposure	Radiological TNM stage	outcome at the end of chemotherapy mRECIST	Evaluation of the response to chemotherapy
1	M/72	Epitheloid	1	Professional	T2N1M0	PD	PD
2	F/71	Biphasic	1	Professional	T3N0M0	PD	PD
3	M/52	Epitheloid	2	Professional	T1bN1M0	PD	PD
4	M/62	Epitheloid	1	Professional	T3N2M0	PD	PD
5	M/73	Epitheloid	1	Professional	T4N3M0	ST	DC
6	F/75	Epitheloid	4	Not known	T3N0M0	PR	DC
7	M/58	Epitheloid	1	Environmental	T3N2M0	ST	DC
8	M/75	Epitheloid	1	Professional	T3N0M0	PR	DC
9	F/46	Biphasic	1	Environmental	T3N2M0	ST	DC
10	M/61	Epitheloid	1	Professional	T2N0M0	ST	DC
11	M/67	Sarcomatoid	2	Professional	T4N0M0	ST	DC
12	M/60	Epitheloid	1	Not known	T1bN0M0	ST	DC
13	M/75	Epitheloid	1	Professional	T3N0M0	ST	DC
14	M/68	Epitheloid	2	Professional	T3N0M0	PD	PD
15	M/84	Epitheloid	1	Environmental	T2N0M0	PD	PD
16	M/60	Epitheloid	1	Professional	T3N2M0	ST	DC
17	M/72	Epitheloid	2	Professional	T4N1M0	ST	DC
18	M/80	Epitheloid	1	Professional	T4N0M0	ST	DC
19	M/67	Epitheloid	4	Not known	T4N0M0	ST	DC

Note: mRECIST = modified Response Evaluation Criteria in Solid Tumors, PD = progressive disease, ST = stable disease, PR = partial response, DC = disease control.

4.1 Comparison Analysis of DCE Parameters Between the Two Models

DCE parameter values differed between the two models. The v_p values differed in all measurements. The K^{trans} and v_e values roughly correlated. The AUC values correlated most frequently; precisely in 7 patients in the pre-treatment study, 8 patients in the intra-treatment study and 8 patients in the post-treatment study. Detailed results are presented in Table 4.2.

Table 4.2: Comparison of the DCE parameters between the two models (K^{trans}, k_{ep}, AUC, v_p, and v_e).

	Pre-treatment study					Intra-treatment study					Post-treatment study				
Patient No.	K^{trans}	k_{ep}	AUC	v_p	v_e	K^{trans}	k_{ep}	AUC	v_p	v_e	K^{trans}	k_{ep}	AUC	v_p	v_e
1	+	-	-	+	+	+	+	+	+	+	+	+	+	+	+
2	+	+	+	+	-	+	+	-	+	+	+	+	-	+	+
3	+	+	-	+	+	+	+	+	+	+	+	+	+	+	+
4	+	+	+	+	+	+	+	+	+	+	+	+	+	+	+
5	+	+	-	+	+	+	+	+	+	+	+	+	+	+	+
6	+	+	-	+	+	+	+	-	+	+	+	+	-	+	+
7	+	+	+	+	+	+	+	+	+	+	+	+	+	+	+
8	+	+	+	+	+	+	+	-	+	+	+	+	-	+	+
9	+	+	+	+	+	+	+	+	+	+	+	+	+	+	+
10	+	+	+	+	+	+	+	+	+	+	+	+	-	+	-
11	+	+	-	+	+	+	+	-	+	-	+	+	-	+	+
12	+	+	+	+	+	+	+	-	+	+	+	+	+	+	+
13	+	+	+	+	+	+	+	+	+	+	+	+	-	+	+
14	+	+	+	+	+	+	+	+	+	+	+	+	+	+	+
15	+	+	-	+	-	+	-	+	+	+	+	+	-	+	+
16	+	+	+	+	+	+	+	+	+	+	-	+	+	+	-
17	+	+	+	+	+	-	+	-	+	+	+	+	+	+	+
18	+	+	-	+	+	+	+	-	+	+	+	+	+	+	+
19	+	+	+	+	+	+	+	-	+	+	+	+	-	+	+

Note: "-" indicates the P value > .05 and, "+" the P value < .05, Ktrans (1/min), kep (1/min), AUC (mM), v_e (ml/100ml),v_p (ml/100 ml)

In Bland-Altman agreement plot, a small negative mean difference of -0.02 (95% CI -0.04 to 0.009) was observed between the K^{trans} values with the two outliers found beyond the lower line, showing a tendency for higher bias in tumors with high permeability (see Figure 4.1a).

A small negative difference of -0.08 (95% CI -0.14 to -0.02) was observed in k_{ep} values with two points found close to the lower line of agreement (see Figure 4.1b). This shows that k_{ep} values are generally interchangeable with the caveat that in tumors with increased k_{ep} values, the ET model seems to overestimate the parameter relatively to the AATH.

An increasing difference between the two models was observed in v_p values with one outlier extending beyond the upper limit of agreement, thus the v_p parameters are not interchangeable between the models (see Figure 4.1c).

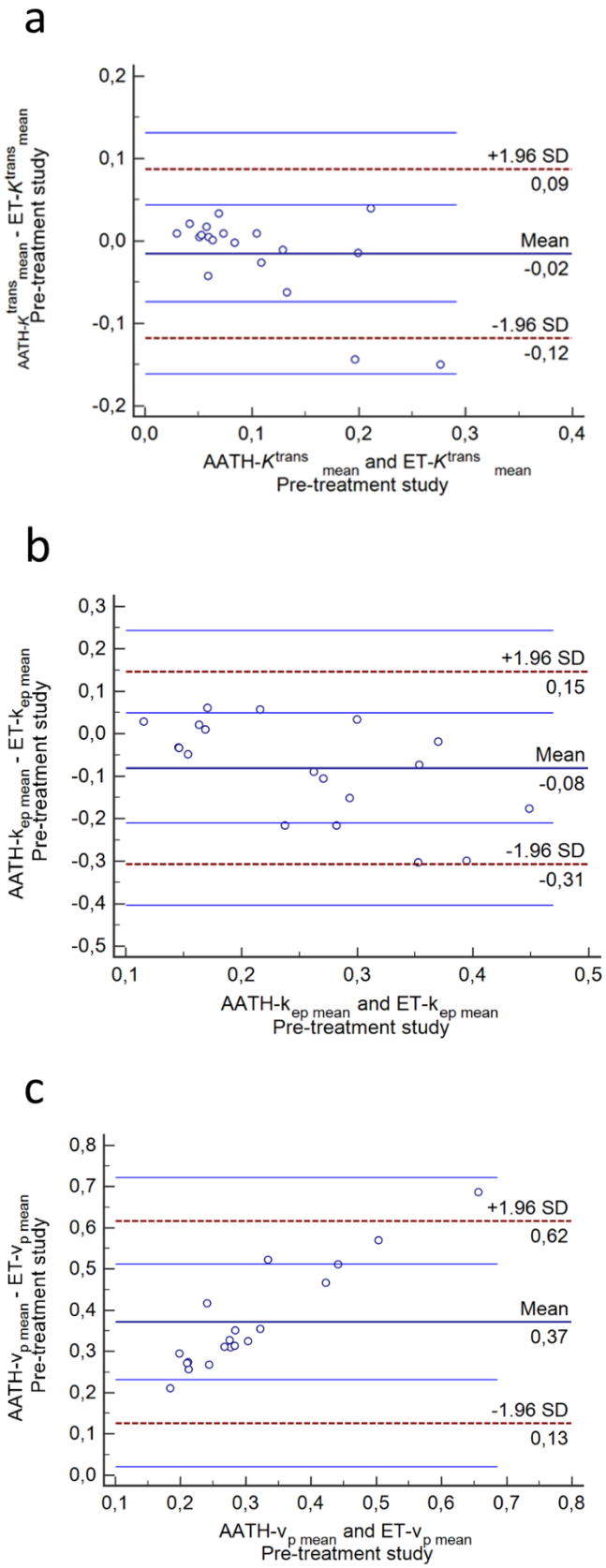

Figure 4.1: Bland-Altman agreement plot of the mean values of the DCE parameters in the pre-treatment study. Top and bottom dashes show 95% of agreement, middle line

shows mean difference. a) transfer constant K^{trans} value (1/min); b) efflux rate constant k_{ep} values (1/min); c) plasma volume v_p values (ml/100 ml)

4.2 Descriptive Statistics and Comparison Analysis of DCE Parameters in Both Models During the Chemotherapy

There was no statistically significant difference in the DCE values calculated using both models during the course of chemotherapy (see Table 4.3).

Table 4.3: Paired sample t test mean difference of the DCE parameters between pre- vs. intra-treatment study and between intra- vs. post-treatment study.

Parameters	Intra- vs. pre-treatment study, mean +/-SD (p-value)	Post- vs. intra-treatment study, mean +/- SD (p-value)
ET-K^{trans}_{max}	-0.001 +/- 0.06 (>.05)	0.002 +/- 0.3 (>.05)
AATH-K^{trans}_{max}	-0.02 +/- 0.06 (>.05)	-0.06 +/- 0.2 (>0.05)
ET-$k_{ep\ max}$	-0.1 +/- 0.5 (>.05)	0.05 +/- 0.8 (>.05)
AATH-$k_{ep\ max}$	0.1 +/- 1.6 (>.05)	- 0.2 +/- 1.7 (>.05)
ET-AUC $_{max}$	-5062 +/- 26775 (>.05)	-9783 +/- 29591 (>.05)
AATH-AUC $_{max}$	-3310 +/- 27804 (>.05)	-9606 +/- 25440 (>.05)
ET-$v_{p\ max}$	- 0.01 +/- 0.3 (>.05)	-0.04 +/- 0.3 (>.05)
AATH-$v_{p\ max}$	0	0
ET-$v_{e\ med}$	0.009 +/- 0.2 (>.05)	-0.05 +/-0.3 (>.05)
AATH-$v_{e\ med}$	0.07 +/- 0.2 (>.05)	-0.09 +/- 0.4 (>0.05)
$T_{C\text{-}max}$	6 +/- 62. (>.05)	-4 +/- 68 (>.05)
$E_{\text{-}max}$	0.009 +/- 0.02 (>.05)	-0.005 +/- 0.02 (>.05)
$F_{p\text{-}max}$	-10 +/- 34 (.05)	40 +/- 168 (>.05)

Note: K^{trans} (1/min), k_{ep} (1/min), AUC (mM), v_e (ml/100ml), v_p (ml/100 ml), TC (min), F (ml/min/100 ml), E (%).

The maximal ET-calculated k_{ep} values at pre-treatment study were significantly different between the group of PD and DC after the third cycle of chemotherapy (P = 0.01) and post-treatment (P = 0.04). Specifically, maximal pre-treatment ET-calculated k_{ep} values were higher by 41% in a DC group. Also, median AATH-calculated pre-treatment k_{ep} values were significantly different between the group of PD and DC post-treatment (P = 0.019) and were higher by 61% in DC group. Additionally, there was a similar difference when we compared mean AATH-calculated pre-treatment k_{ep} values between the group of PD and DC post-treatment (P = 0.015) (see Table 4.4). Correlation of other values was not statistically significant.

Table 4.4: Paired sample t test of the mean values of the DCE parameters (K^{trans}, k_{ep}) between disease control and progressive disease group.

Perfusion parameter	Disease control group	Progressive disease group	p-value
Pre-treatment study			
ET-K^{trans} $_{mean}$	0.12	0.08	0.54
AATH-K^{trans} $_{mean}$	0.12	0.07	0.23
ET-$k_{ep\ mean}$	0.33	0.24	0.19
AATH-$k_{ep\ mean}$	0.33	0.20	0.015
Intra-treatment study			
ET-K^{trans} $_{mean}$	0.10	0.11	0.36
AATH-K^{trans} $_{mean}$	0.12	0.08	0.21
ET-$k_{ep\ mean}$	0.28	0.35	0.31
AATH-$k_{ep\ mean}$	0.26	0.19	0.35
Post-treatment study			
ET-K^{trans} $_{mean}$	0.10	0.08	0.82
AATH-K^{trans} $_{mean}$	0.08	0.07	0.58
ET-$k_{ep\ mean}$	0.36	0.27	0.76
AATH-$k_{ep\ mean}$	0.25	0.20	0.82

Note: K^{trans} (1/min), k_{ep} (1/min).

The changes in the maximal values of K^{trans} and k_{ep} are shown in Figure 4. The dynamics of change in ET-calculated maximal K^{trans} values in DC group present a slight increase intra-treatment, followed by a pronounced decrease post-treatment. K^{trans} values in PD group showed a marked increase intra-treatment followed by a decrease post-treatment (see Figure 4.2a).

The AATH-calculated maximal K^{trans} values showed slight but continuous reduction during treatment in both DC and PD group (see Figure 4.2b).

The ET-calculated maximal k_{ep} values in DC group initially decreased, followed by a slight rebound. In PD group, the values showed increased intra-treatment, followed by a decrease post-treatment (see Figure 4.2c).

The AATH-calculated median k_{ep} values in PD group showed an increase intra-treatment followed by a decrease post-treatment. In DC group, a persistent decrease in the values was observed (Fig. 2d).

AUC values using both models continuously but non-significantly decreased during the chemotherapy in DC group, whereas in PD group there was a slight increase in the first phase of the treatment, followed by a pronounced decrease in the second phase of the treatment (see Figure 4.2e and 4.2f).

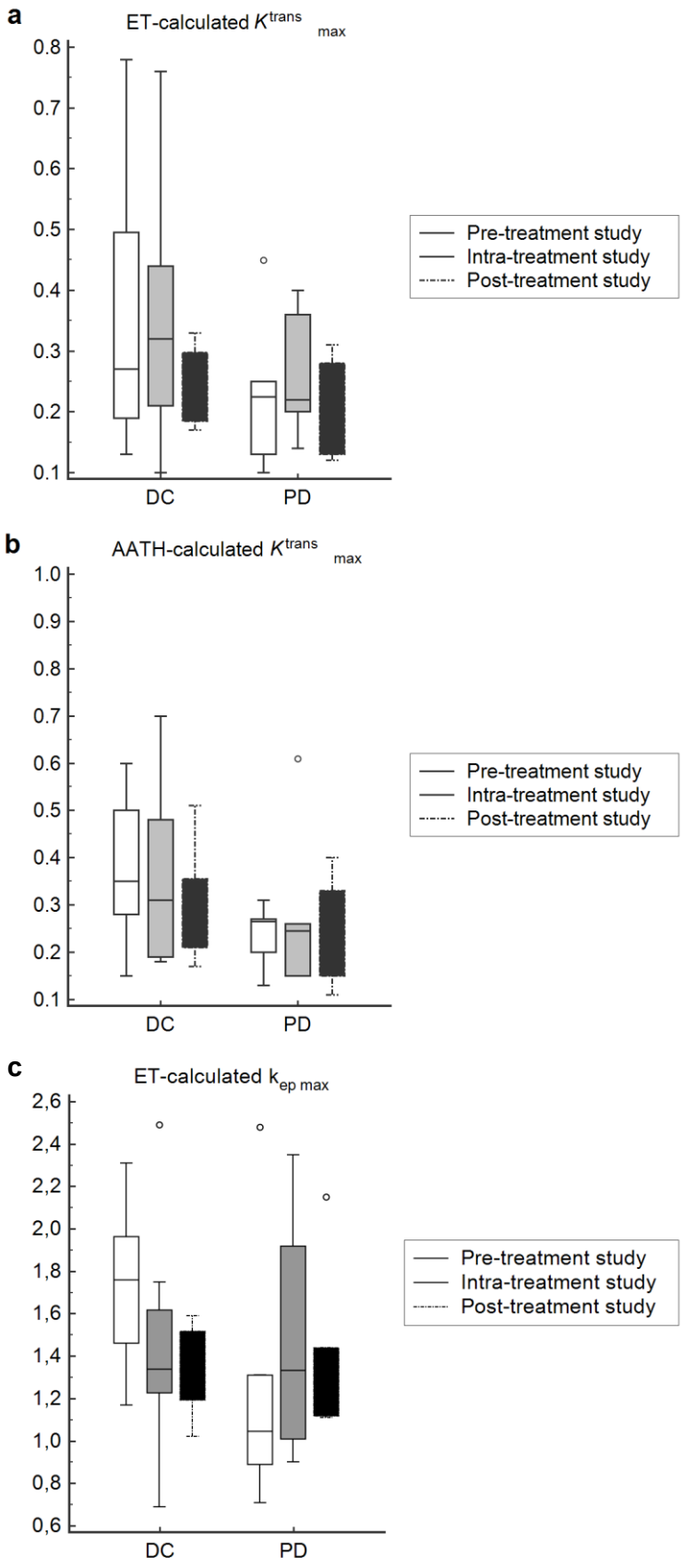
a
ET-calculated K^{trans}_{max}
0.8
0.7
0.6
0.5
0.4
0.3
0.2
0.1
DC
PD
Pre-treatment study
Intra-treatment study
Post-treatment study
b
AATH-calculated K^{trans}_{max}
1.0
0.9
0.8
0.7
0.6
0.5
0.4
0.3
0.2
0.1
DC
PD
Pre-treatment study
Intra-treatment study
Post-treatment study
c
ET-calculated $k_{ep\ max}$
2,6
2,4
2,2
2,0
1,8
1,6
1,4
1,2
1,0
0,8
0,6
DC
PD
Pre-treatment study
Intra-treatment study
Post-treatment study

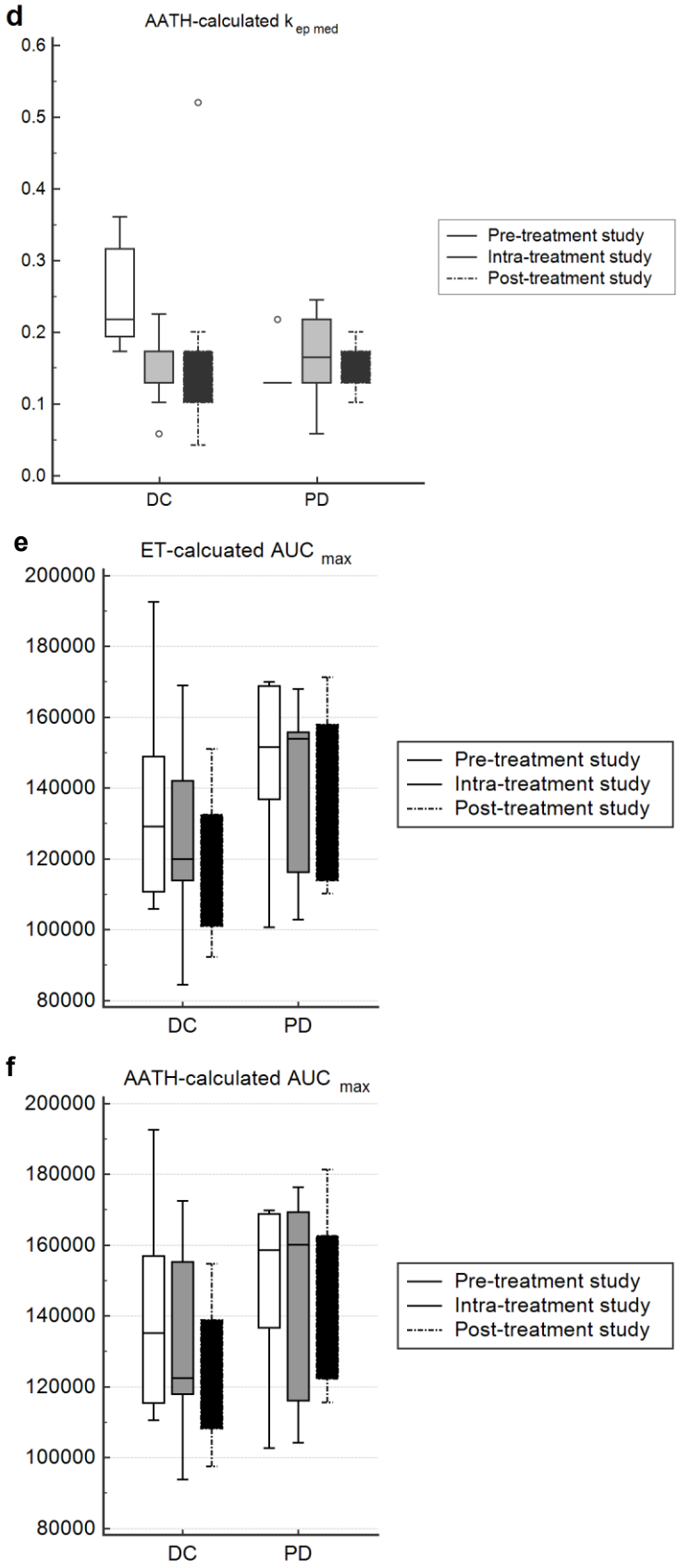

Figure 4.2: The dynamics of K^{trans} and k_{ep} values calculated using both models during the course of the chemotherapy. Box represents interquartile range, the line dividing the box

indicates the median and circles represent the outliers. a) ET-calculated $K^{trans}{}_{max}$ values, b) AATH-calculated $K^{trans}{}_{max}$ values, c) ET-calculated $k_{ep\ max}$ values, d) AATH-calculated $k_{ep\ med}$ values, e) ET-calculated AUC $_{max}$ values, f) AATH-calculated AUC $_{max}$ values. Figures 4.3 to 4.5 present k_{ep} parametric maps in three patients, one with PD, PR and SD according to mRECIST.

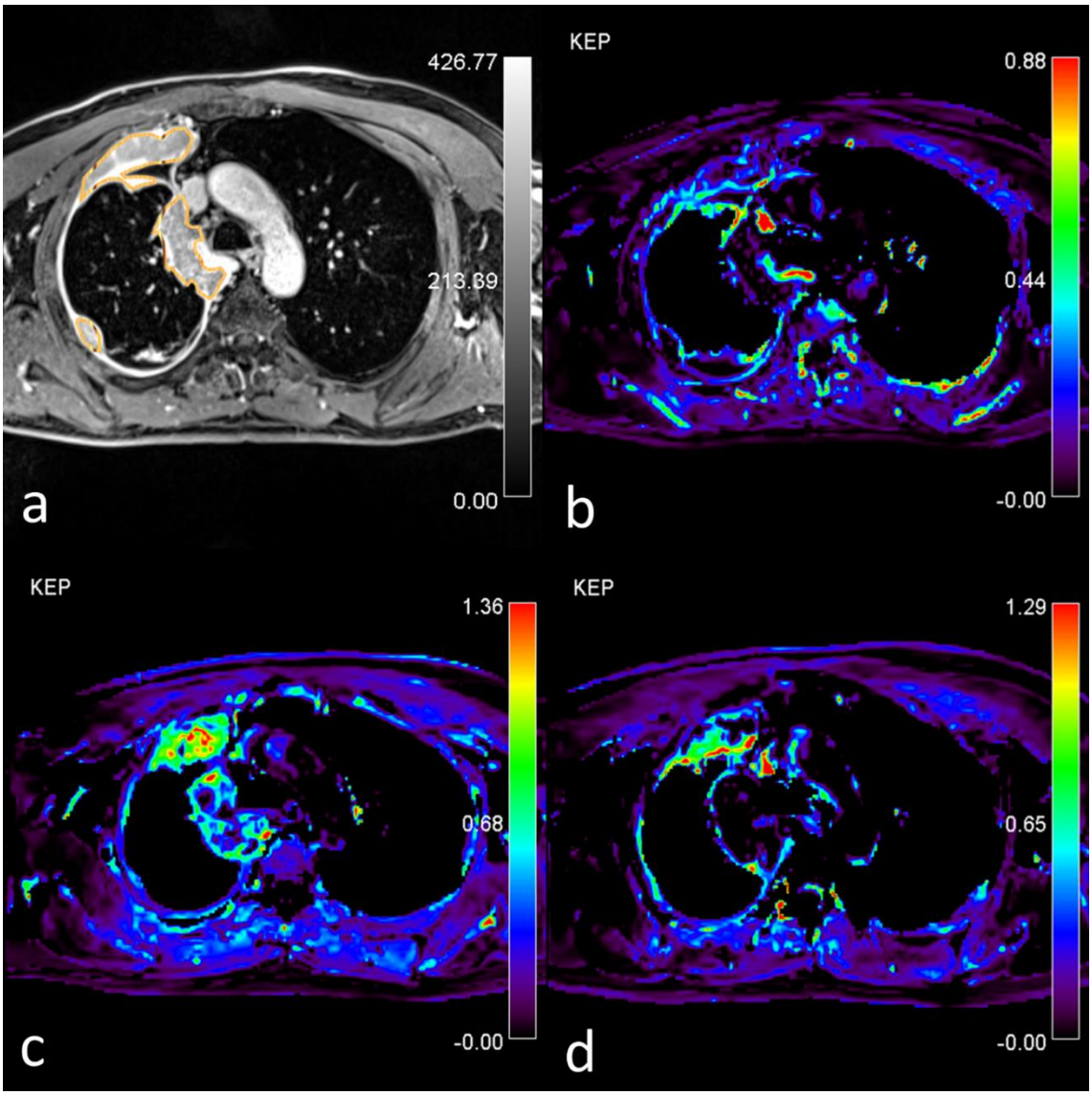

Figure 4.3: Patient with progressive disease. a) Post-contrast T1-weighted turbo-FLASH. Source image shows the region of interest (ROI) drawn around the tumor, AATH-calculated k_{ep} parametric map (1/min) from b) pre-treatment, c) intra-treatment, and d) post-treatment study is shown. At the intra-treatment study, tumor showed an increase in k_{ep} as well as in size. At the post-treatment study, a decrease in k_{ep} and a slight increase in tumor size is seen. Significant heterogeneity of the tumor can be observed.

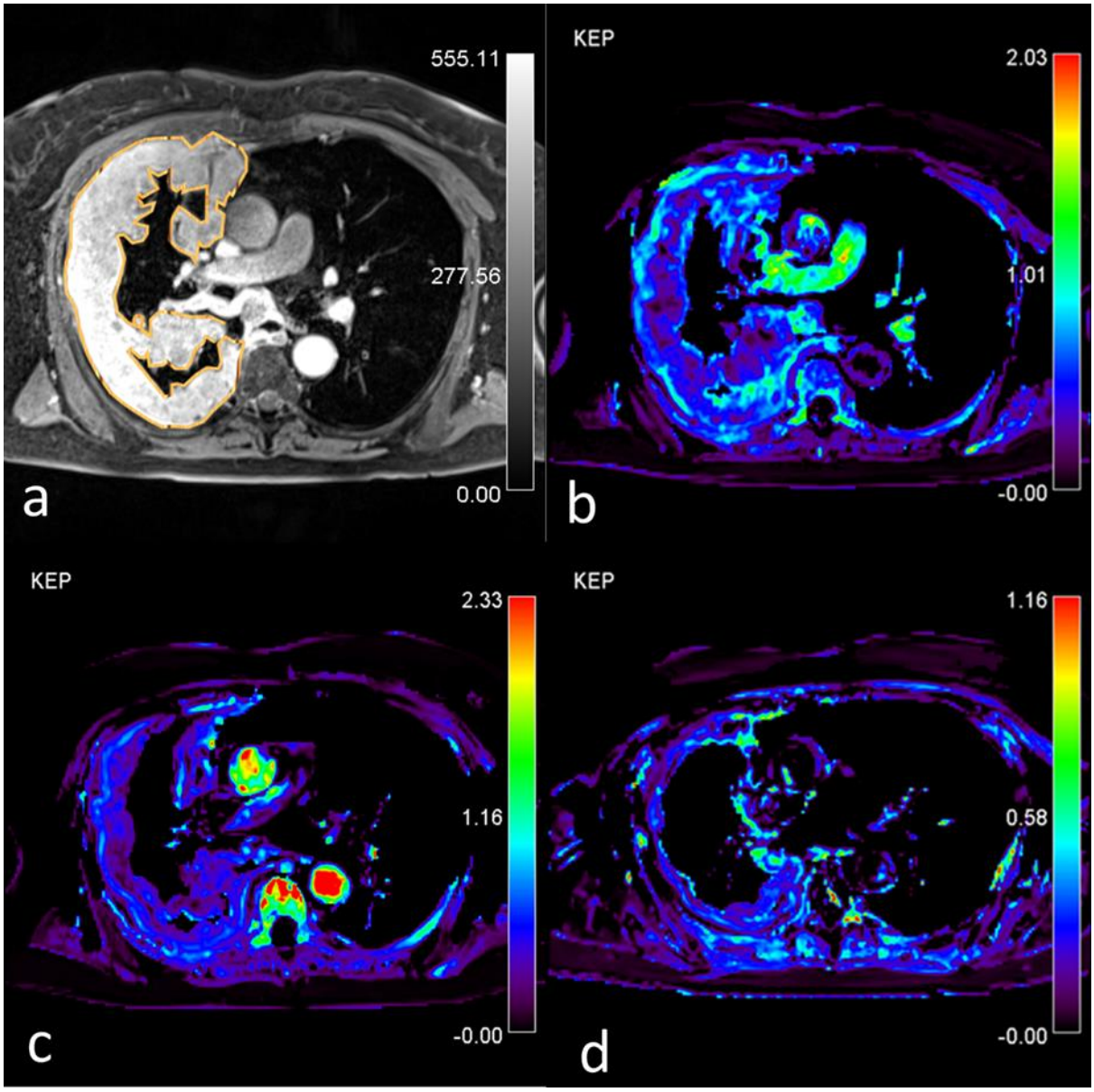

Figure 4.4: Patient with partial response. a) Post-contrast T1-weighted turbo-FLASH. Source image shows the region of interest (ROI) drawn around the tumor, AATH-calculated k_{ep} parametric map (1/min) from b) pre-treatment, c) intra-treatment, and d) post-treatment study is shown. Tumor reduced in size which was flowed by a reduction in the k_{ep} during the course of chemotherapy. The distribution of the k_{ep} is spatially heterogeneous with high values in the periphery and low values in the core.

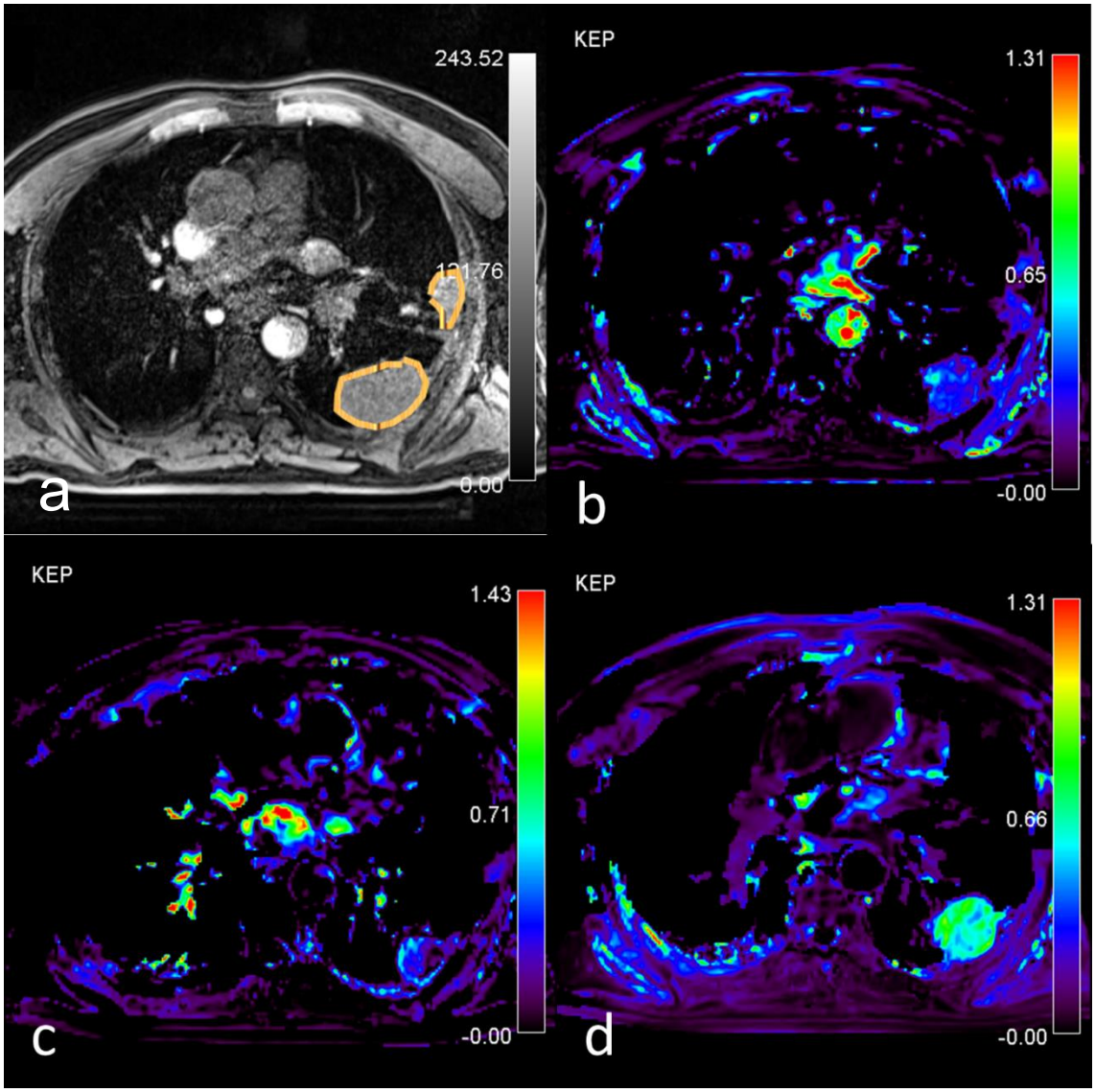

Figure 4.5: Patient with stable disease. a) Post-contrast T1-weighted turbo-FLASH. Source image shows the region of interest (ROI) drawn around the tumor, AATH-calculated k_{ep} parametric map (1/min) from b) pre-treatment, c) intra-treatment, and d) post-treatment study is shown. Tumor remained almost the same size during the treatment which was accompanied by stable k_{ep} values.

4.3 ROC Curve Analysis

The ROC curve analysis showed a significant predictive value of maximal pre-treatment ET-calculated k_{ep} values for MPM response during treatment with estimated sensitivity and specificity of 100% ($P < 0.001$; cut-off of ≥ 0.89 /min, AUC 1). However, the maximal pre-treatment ET-calculated k_{ep} values were less predictive for the MPM response after finishing the chemotherapy with estimated sensitivity and specificity of 83.3% and 92.3%, respectively ($P = 0.06$; cut-off of ≥ 1.31 /min, AUC 0.81) (see Figure 4.6a). ROC curve analysis also showed a significant predictive value of median pre-treatment AATH-calculated k_{ep} values for MPM response during the treatment with estimated sensitivity of 100% and specificity of 82% ($P < 0.0001$; cut-off of ≥ 0.13 /min, AUC 0.91) and post-

treatment with estimated sensitivity of 83,3% and specificity of 100% ($P < 0.0001$; cut-off of ≥ 0.13 /min, AUC 0.92) (see Figure 4.6b). Other DCE parameters values showed no predictive value for MPM response to therapy (see Table 4.5 and 4.6).

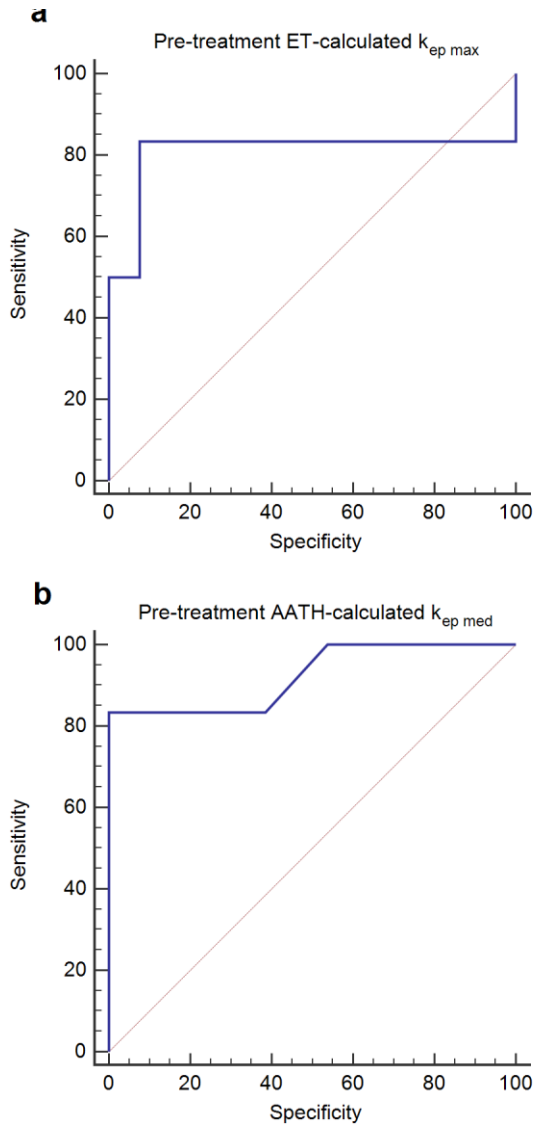

Figure 4.6: ROC of k_{ep} values for predicting tumor response to chemotherapy.

a) ET-calculated k_{ep} values b) AATH-calculated k_{ep} values. Both ET- and AATH-calculated k_{ep} values show significant predictive value in predicting MPM treatment response.

Table 4.5: ROC curve analysis of the DCE parameters for the inter-treatment tumor response to chemotherapy.

Parameters	Cut off	AUC	*P*	Sensitivity %	Specificity %	Positive LR	Negative LR
ET-K^{trans}_{max}	≥0.08	0.68	0.31	100	52.9	2.12	0
AATH-K^{trans}_{max}	≥0.09	0.62	0.60	100	41.2	1.70	0
ET-$k_{ep\ max}$	≥0.89	1	**<0.001**	100	100		0
AATH- $k_{ep\ max}$	≥0.95	0.62	0.76	50	100		0.50
AATH-$k_{ep\ med}$	≥0.13	0.91	**<0.001**	100	82.4	5.67	0
ET-AUC max	≥136823	0.77	0.27	100	52.9	2.12	0
AATH-AUC $_{max}$	≥136784	0.77	0.27	100	52.9	2.12	0
ET-$v_{p\ max}$	<0.79	0.76	0.09	100	64.7	2.83	0
AATH-$v_{p\ max}$	NA	NA	NA	NA	NA	NA	NA
ET-$v_{e\ med}$	<0.35	0.65	0.22	100	64.7	2.83	0
AATH-$v_{e\ med}$	<.35	0.65	0.22	100	64.7	2.12	0
TC-$_{max}$	≥539	0.63	0.30	100	47.1	1.42	0.77
E-$_{max}$	≥0.92	0.72	0.38	50	94.1	8.50	0.53
F_p-$_{max}$	<533	0.71	0.09	100	73	8.50	0

Note: the statistically significant and borderline significant values (P≤.05) are set in bold. K^{trans} (1/min), k_{ep} (1/min), AUC (mM), v_e (ml/100ml),v_p (ml/100 ml), TC (min), F (ml/min/100 ml), E (%), NA=not applicable

Table 4.6: ROC curve analysis of the DCE parameters for the post-treatment tumor response to chemotherapy.

Parameters	Cut off	AUC	*P*	Sensitivity %	Specificity %	Positive LR	Negative LR
PRE-TREATMENT STUDY							
ET-K^{trans}_{max}	<0.14	0.5	1	0	69.2	0	1.44
AATH-K^{trans}_{max}	≥0.09	0.59	0.53	83.3	46.2	1.55	0.36
ET-$k_{ep\ max}$	≥1.31	0.81	0.06	83.3	92.3	10.83	0.18
AATH-$k_{ep\ max}$	≥1.21	0.67	0.32	50	100		0.50
AATH-$k_{ep\ med}$	≥0.13	0.932	**<0.0001**	83.3	100		0.17
ET-AUC $_{max}$	<129926.96	0.67	0.29	83.3	61.5	2.17	0.27
AATH-AUC $_{max}$	<136508.6	0.68	0.26	83.3	61.5	2.17	0.27
ET-$v_{p\ max}$	<0.62	0.76	0.09	100	61.5	2.60	0
AATH-$v_{p\ max}$	NA	NA	NA	NA	NA	NA	NA
ET-$v_{e\ med}$	<0.28	0.57	0.57	83.3	53.8	1.81	0.31
AATH-$v_{e\ med}$	<0.57	0.5	1	0	69.2	0	1.44
T_{C}-$_{max}$	≥575.78	0.53	0.81	83.3	30.8	1.20	0.54
E-$_{max}$	≥0.92	0.67	0.11	33.3	100		0.67
F_{p}-$_{max}$	<533.42	0.71	0.09	66.7	100		0.33
INTRA-TREATMENT STUDY							
ET-K^{trans}_{max}	≥0.36	0.66	0.23	83.3	50	1.67	0.33
AATH-K^{trans}_{max}	≥0.26	0.70	0.19	83.3	66.7	2.50	0.25
ET-$k_{ep\ max}$	<1.01	0.50	1	66.7	9.1	0.73	3.67
AATH-$k_{ep\ max}$	<1.09	0.54	0.76	100	27.3	0.37	0
ET-AUC $_{max}$	<138567	0.63	0.43	66.7	76.9	2.89	0.43
AATH-AUC $_{max}$	<138219	0.60	0.55	66.7	69.2	2.17	0.48
ET-$v_{p\ max}$	≥0.72	0.61	0.42	83.3	53.8	1.81	0.31
AATH-$v_{p\ max}$	NA	NA	NA	NA	NA	NA	NA
ET-$v_{e\ med}$	≥0.47	0.61	0.40	100	30.8	1.44	0
AATH-$v_{e\ med}$	≥0.58	0.64	0.30	100	41.7	1.71	0
T_{C}-$_{max}$	≥539.85	0.64	0.36	83.3	58.3	2.00	0.29
E-$_{max}$	≤1	0.5	1	0	100		1
F_{p}-$_{max}$	≥378.76	0.64	0.32	83.3	58.3	2.00	0.29

Note: the statistically significant and borderline significant values (P≤.05) are set in bold. K^{trans} (1/min), k_{ep} (1/min), AUC (mM), v_e (ml/100ml),v_p (ml/100 ml), TC (min), F (ml/min/100 ml), E (%), NA=not applicable

Chapter 5

Discussion

Imaging plays a central role in the management of cancer patients. Alongside diagnostics, it is used for staging, treatment monitoring, detection of recurrence or surveillance. The crucial role of modern imaging is the detection of tumor changes early during the treatment to identify early response failure prompting for second line treatment in a timely manner. Hence, the development of reliable and robust imaging biomarkers that would give information on tumor biology and tumor changes in response to therapy is of paramount importance for personalized tumor treatment.

MPM has been causally linked to asbestos exposure in many epidemiological studies (Franko et al., 2012). In our patient cohort 84% remember being exposed to asbestos, most of them professionally. MPM has a long latency period, from 15 to 60 years. Its incidence is increasing and the peak is expected in 2020 (Giesel et al., 2006; Scherpereel, Astoul, Baas, Berghmans, Clayson, de Vuyst, Dienemann, Galateau-Salle, Hennequin, Hillerdal, Le Péchoux et al., 2010). MPM is a heterogeneous tumor type with three major subtypes – epitheloid, sarcomatoid and bifasic – while other variants occur sporadically. Because different histopathological types show different chemosensitivity, the development of effective chemotherapy is challenging (Robinson, Musk, & Lake, 2005). This has highlighted the need to map the functional and imaging tumor properties that could guide patient stratification and selection of the best available treatment regime. DCE-MRI is a promising tool that can provide quantitative and functional parameters for assessing tumor vascularity. We evaluated the use of DCEI in the evaluation of MPM response to therapy (Vivoda Tomsic, Bisdas, Kovac, Sersa, & Surlan Popovic, 2019).

Our patients were enrolled under the currently conventional treatment scheme which included cisplatin with pemetrexed or gemicitabine. Gemcitabine and pemetrexed are both cytotoxic agents, whereas cisplatin has a cytotoxic and anti-angiogenic compound (Gandhi et al., 2006). It has been noted that cytostatics may exert change on tumor vasculature and interfere with angiogenic cascade without causing endothelial cell death (Padhani et al., 2006; Tudorica et al., 2016). Based on this treatment effect, we were inclined to use the perfusion MRI-derived biomarkers as a surrogate for monitoring the treatment-related vascular changes. To start with, we attempted to address any ambiguity for the most accurate capture of the underlying pathophysiology using the current state-of-the-art DCE tracer kinetic models. ET model is broadly established because of its robustness and rather simple computational demand, but AATH presents a more elaborate though computationally demanding tracer kinetic modeling approach with the prerequisite of sufficient raw data quality. Maybe not surprisingly, quantitative DCE parameters were significantly different between the two models. Only AUC values, which is a lump quantitative parameter reflecting the complex gadolinium behavior of synchronous flow, permeability and compartmental volumes features of the tumor under investigation,

correlated in around half of the patients in all studies, a finding consistent with previously published studies (Donaldson et al., 2010).

Nevertheless, since there is no consensus regarding the choice of the most appropriate model, a pragmatic approach to start using DCE as a therapy monitoring tool is to estimate the magnitude of difference between the two broadly used models. Slight difference might be acceptable across different centers, though it is strongly recommended to use the same model within the same institution and patient surveillance, but more profound differences would flag up this caveat in future studies. Bland-Altman agreement plot analysis, an established method to detect the agreement levels between two different measurements, showed that baseline DCE parameters are satisfactorily interchangeable between the two models only in tumors with a fairly low perfusion and low neo-vascularity. In highly vascularized tumors, the AATH-calculated v_p values were notably higher compared to the ET-calculated model values and there was a tendency for increasing difference in K^{trans} and k_{ep} parameter values. This is consistent with the previously reported studies, where the authors suggested that the ET model may underestimate v_p and overestimate K^{trans} parameter (Kershaw & Cheng, 2010).

We also evaluated the dynamics in DCE parameters during the course of chemotherapy. The results demonstrate no significant difference in DCE parameters. Contrary to the observations in other studies (Kiessling, Jugold, Woenne, & Brix, 2007), K^{trans} values show a slight decline during the first phase of the treatment in both models, followed by a slight decrease in the ET model and slight increase in the AATH model in the second phase of the treatment. The physiological meaning of K^{trans} can be difficult to interpret in a straightforward manner. K^{trans} values may reflect changes in the vessel wall permeability or changes in blood flow, depending on the predominant effect (either much higher K^{trans} or significant high flow) with uncertainly residing in the ET model in case of similar values in these parameters (Koh et al., 2011). During any antiangiogenic treatment, a decrease in vascular permeability is expected due to normalization of leaky neo-vessels, which can be observed as a decrease of K^{trans} values (Kiessling et al., 2007). Our patients in the DC group, ET-calculated K^{trans} values in the early phase of the treatment showed a slight increase, followed by a decrease in the second phase of the treatment. Interval increase or stable values of K^{trans} can be found in non-responsive tumors (Wasser et al., 2003; Yu, Chen, Mehta, Nalcioglu, & Su, 2007). High K^{trans} values, in a setting where K^{trans} predominantly reflects blood flow, are however believed to improve drug delivery and treatment response, as observed in other tumors such as head and neck cancers, glioblastoma and breast cancers (Bisdas, Smrdel, Bajrovic, & Surlan-Popovic, 2016; Brix, Griebel, Kiessling, & Wenz, 2010; Sorensen et al., 2012). AUC values using both models continuously decreased in DC group during the chemotherapy, compared to PD group. AUC has been proposed as a primary end point alternative to K^{trans} for assessing the effect of anti-angiogenic therapy as it does not require model fitting and is relatively robust (Galbraith, 2006).

The current clinical practice is to measure the change in tumor diameter according to mRECIST which is supposed to reflect the tumor overall size change due to treatment. However, the limitation of morphologic approach is that it reflects only the tumor size change due to cell death; it can even be nonspecific (e.g. enlargement post immunotherapy). In novel targeted chemotherapies with cytostatic effect, the size change manifests only after several treatments, when the effect of the treatment can be evaluated. Functional changes antecede morphological size changes. DCE-MRI has been utilized to study the effect of anti-vascular and anti-angiogenic targeted therapy. The reduction in perfusion parameters, specifically the AUC values and K^{trans} values, has been noted up to several hours after application. Thus, the use of DCE-MRI technique may provide an insight into the instant tumor functional response. It has also been used in research to test the dose and the

schedule of the therapy as well as frequent DCE-MRI measurements in research studies were used to help guide the follow-up timeline in clinical trials. Functional imaging with PET/CT is used to demonstrate the tumor metabolism. The standard uptake value (SUV), which is a semiquantitative measure of metabolic activity of a lesion, is high in MPM reflecting high metabolic rate of the tumor. High SUV is usually associated with a poor prognosis. A study in lung cancers has shown that early SUV decrease can reflect response to therapy (Nishino, Hatabu, Johnson, & McLoud, 2014).

Pre-treatment ET and AATH-calculated k_{ep} values were shown to predict the treatment response during and after chemotherapy. In this study, k_{ep} showed an interval decrease in the DC group. A decrease in k_{ep} was either due to the increase in v_e or increase in K^{trans} values. Both phenomena can be attributed to damages to the tumor cells as a result of cytotoxic and the concurrent anti-angiogenic action. The values of v_e using both models were increasing in the DC group and decreasing in the PD group. Cell death may reflect as an increase in v_e and more chaotic tissue architecture (Tudorica et al., 2016). In PD group, k_{ep} values continuously increased in both models, while K^{trans} values were stable or slightly decreasing, reflecting persistent high permeability as a predominant angiogenic feature. In other words, though any cytostatic effect might be present, the persistent angiogenesis drives the tumor resistance to the applied therapy. This finding may suggest that adding an anti-angiogenic substance in the therapeutic regiment may reverse the unfavorable outcome. A study by Ohta et al. has shown that MPM cell lines show higher expression levels of vascular endothelial growth factor (VEGF) compared to normal pleural tissue (Ohta et al., 1999). VEGF is one of the most powerful endothelial cell mitogens and therefore plays a crucial role in neoangiogenesis. It stimulates the proliferation of endothelial cells, induces vasodilatation, permeability of microvessels and the formation of primitive blood vessels (Strizzi et al., 2001). The addition of anti-angiogenic agents in the treatment scheme has been tested in clinical trials. In the largest phase III study, bevacizumab has been added to pemetrexed and cisplatin chemotherapy scheme in a first-line MPM treatment. Bevacizumab is an anti-VEGF monoclonal antibody that binds to soluble VEGF, preventing receptor binding and inhibiting endothelial cell proliferation and vessel formation. It has been the first anti-angiogenic treatment approved by the American Food and Drug Administration in 2004 for the first-line treatment in metastatic colorectal cancer and is now used for treatment of other malignancies. The study has shown that patients enrolled in the novel treatment scheme had a longer overall survival time of median 18.8 months compared to 16.1 months standard of care. VEGF overexpression was associated with worse prognosis, as in some other tumors (Zalcman et al., 2016). Nintedanib is another targeted agent against VEGF receptors. It has also been added to pemetrexed and cisplatin chemotherapy scheme in a first line MPM treatment and patients benefited from longer time to progression. Both clinical trials add to the growing evidence of an additional value of VEGF-targeted therapy to standard chemotherapy (de Gooijer, Baas, & Burgers, 2018).

We observed spatial heterogeneity of MPM on the perfusion maps. Unlike in other tumors, MPM spatial and temporal heterogeneity has not been described in histopathological studies. DCE-MRI opens up the possibility to demonstrate different phases of angiogenesis and tumor vessel permeability in MPM. It has been described in other tumors such as breast cancers, prostate cancers and glioblastoma (Choyke, Dwyer, & Knopp, 2003). Tumor heterogeneity contributes to worse prognosis due to mixed response to chemotherapy. We chose to perform the descriptive statistics and comparison analysis of DCE parameters in both models during the chemotherapy. Maximum perfusion values were used due to the fact that they reflect the most malignant properties of the MPM.

A study by Giesel et al. was published on the use of DCE-MRI to assess the effect of chemotherapy in MPM where Brix model was used for analysis (Giesel et al., 2008). Similar to the simplified Tofts model, plasmatic compartment in Brix model is neglected and only the v_e compartment is considered. Exchange rate constant between the extravascular and vascular compartment (k_{ep}) in Brix model can be compared to k_{ep} parameter assessed by the ET and AATH model. As in our study, responders demonstrated a decrease in k_{ep} values, and non-responders demonstrated an increase in k_{ep} values during treatment. Giesel et al. attributed that to the proportion of the contrast agent distribution in the tissue of interest - Amp, which is significantly higher in MPM compared to normal tissue, as in high vascularized tissue. In another study by Giesel and coworkers, immunohistochemistry was used and high microvascular density in MPM was demonstrated (Giesel et al., 2008). This further overwhelmingly justifies our choice to use the ET model, which was developed as an extension to the Tofts model, as a need to account for tumor plasma volume has been recognized (Gordon et al., 2014). The third calculated parameter using Brix model – k_{el} does not allow extrapolation to any parameter assessed with either ET or AATH model.

The first and main limitation, in our opinion, is the relatively small number of patients. This reflects the small incidence of MPM and on top of that not all patients were eligible for chemotherapy due to comorbidity or advanced disease stage. Despite this, the number of patients that have completed the chemotherapy and were scanned is almost three times higher, compared to the only previously published study on the use of DCE-MRI in MPM [4]. Secondly, because of the presence of diffuse pleural growth combined with small tumor foci dictated an extended anatomical coverage in our DCE-MRI experiments limiting the spatial and temporal resolution. Consequently, we chose the most suitable trade-off in order to acquire images with sufficient quality for the subsequent modelling. Reportedly, ET model analysis performs better in relatively low temporal resolution conditions (Ledsam, Hodgson, Moots, & Sourbron, 2013). Thirdly, despite the extended anatomical coverage, not all tumor foci were included in DCE-MRI scans, therefore, tumor heterogeneity was not fully accounted for. Fourthly, our study population consisted of patients in all disease stages with a mature vascular phenotype. The anti-angiogenic chemotherapy effect is believed to be the most effective in disrupting the growth of immature new vasculature (Kiessling et al., 2007). Including patients only in the earlier disease stages could show the maximum therapeutic benefit of the anti-angiogenic effect. Fifthly, instead of using the Tofts model for the DCE analysis, we decided to perform the analysis using the extended Tofts model to account for tumor plasma volume because of the aforementioned high microvascular density in MPM (Giesel et al., 2008; Gordon et al., 2014). Because of the overflow of data and the complexity of the distributed parameter model, we performed the comparison of two models instead of three. Despite that, we proved that the perfusion parameters, calculated using different tracer kinetic models, yield significantly different values. Finally, our endpoints did not include progression and overall survival time.

Chapter 6

Conclusions

Hypothesis 1: We have rejected the hypothesis. There were no statistically significant differences in the perfusion values, calculated using both models, during the course of chemotherapy.

Hypothesis 2: We have rejected the hypothesis. The measured perfusion parameter values differed between the two models; the v_p values differed in all measurements, the K^{trans} and v_e values roughly correlated and the AUC values correlated most frequently.

Hypothesis 3: We have accepted the hypothesis. The maximal k_{ep} values, calculated using the ET model at the pre-treatment study, were significantly different between the group of patients demonstrating stable disease and partial response and the group of patients demonstrating progressive disease according to mRECIST criteria at the intra and post-treatment study. Also, the median and mean k_{ep} values, calculated using the AATH model at the pre-treatment study, were significantly different between the group of patients demonstrating stable disease and partial response and the group of patients demonstrating progressive disease according to mRECIST criteria post-treatment.

Hypothesis 4: We have accepted the hypothesis. The ROC curve analysis showed a significant predictive value of maximal pre-treatment ET-calculated k_{ep} values for MPM response during treatment and a significant predictive value of median pre-treatment AATH-calculated k_{ep} values for MPM response during the treatment and post-treatment.

References

"Perfusion model". (2013). Retrieved from https://www.olea-medical.com/en/documentation/technical-compendium/

Akira, M. (2008). Imaging of occupational and environmental lung diseases. *Clinics in Chest Medicine, 29*(1), 117-31, vi. doi:10.1016/j.ccm.2007.11.001

Armato, S. G.,3rd, Labby, Z. E., Coolen, J., Klabatsa, A., Feigen, M., Persigehl, T., & Gill, R. R. (2013). Imaging in pleural mesothelioma: A review of the 11th international conference of the international mesothelioma interest group. *Lung Cancer (Amsterdam, Netherlands), 82*(2), 190-196. doi:10.1016/j.lungcan.2013.08.005 [doi]

Bisdas, S., Smrdel, U., Bajrovic, F. F., & Surlan-Popovic, K. (2016). Assessment of progression-free-survival in glioblastomas by intratreatment dynamic contrast-enhanced MRI. *Clinical Neuroradiology, 26*(1), 39-45. doi:10.1007/s00062-014-0328-0 [doi]

Brix, G., Griebel, J., Kiessling, F., & Wenz, F. (2010). Tracer kinetic modelling of tumour angiogenesis based on dynamic contrast-enhanced CT and MRI measurements. *European Journal of Nuclear Medicine and Molecular Imaging, 37 Suppl 1*, S30-51. doi:10.1007/s00259-010-1448-7 [doi]

Byrne, M. J., & Nowak, A. K. (2004). Modified RECIST criteria for assessment of response in malignant pleural mesothelioma. *Annals of Oncology : Official Journal of the European Society for Medical Oncology / ESMO, 15*(2), 257-260.

Cemazar, M., Parkins, C. S., Holder, A. L., Chaplin, D. J., Tozer, G. M., & Sersa, G. (2001). Electroporation of human microvascular endothelial cells: Evidence for an anti-vascular mechanism of electrochemotherapy. *British Journal of Cancer, 84*(4), 565-570. doi:10.1054/bjoc.2000.1625

Choyke, P. L., Dwyer, A. J., & Knopp, M. V. (2003). Functional tumor imaging with dynamic contrast-enhanced magnetic resonance imaging. *Journal of Magnetic Resonance Imaging : JMRI, 17*(5), 509-520. doi:10.1002/jmri.10304 [doi]

Clements, M. K., Jones, C. B., Cumming, M., & Daoud, S. S. (1999). Antiangiogenic potential of camptothecin and topotecan. *Cancer Chemotherapy and Pharmacology, 44*(5), 411-416.

Colaiacomo, M. C., Masselli, G., Polettini, E., Lanciotti, S., Casciani, E., Bertini, L., & Gualdi, G. (2009). Dynamic MR imaging of the pelvic floor: A pictorial review. *Radiographics : A Review Publication of the Radiological Society of North America, Inc, 29*(3), e35. doi:10.1148/rg.e35; 10.1148/rg.e35

Cooke, W. E. (1924). Fibrosis of the lungs due to the inhalation of asbestos dust. *British Medical Journal, 2*(3317), 147-140.2.

Coolen, J., De Keyzer, F., Nafteux, P., De Wever, W., Dooms, C., Vansteenkiste, J., . . . Verschakelen, J. (2012). Malignant pleural disease: Diagnosis by using diffusion-weighted and dynamic contrast-enhanced MR imaging--initial experience. *Radiology, 263*(3), 884-892. doi:10.1148/radiol.12110872 [doi]

de Gooijer, C. J., Baas, P., & Burgers, J. A. (2018). Current chemotherapy strategies in malignant pleural mesothelioma. *Translational Lung Cancer Research, 7*(5), 574-583. doi:10.21037/tlcr.2018.04.10 [doi]

Donaldson, S. B., West, C. M., Davidson, S. E., Carrington, B. M., Hutchison, G., Jones, A. P., . . . Buckley, D. L. (2010). A comparison of tracer kinetic models for T1-weighted dynamic contrast-enhanced MRI: Application in carcinoma of the cervix. *Magnetic Resonance in Medicine, 63*(3), 691-700. doi:10.1002/mrm.22217 [doi]

Entwisle, J. (2004). The use of magnetic resonance imaging in malignant mesothelioma. *Lung Cancer (Amsterdam, Netherlands), 45 Suppl 1*, S69-71. doi:10.1016/j.lungcan.2004.04.015

ESMO Guidelines Working Group, & Manegold, C. (2007). Malignant pleural mesothelioma: ESMO clinical recommendations for diagnosis, treatment and follow-up. *Annals of Oncology : Official Journal of the European Society for Medical Oncology / ESMO, 18 Suppl 2*, ii34-5. doi:18/suppl_2/ii34 [pii]

Franko, A., Dolzan, V., Kovac, V., Arneric, N., & Dodic-Fikfak, M. (2012). Soluble mesothelin-related peptides levels in patients with malignant mesothelioma. *Disease Markers, 32*(2), 123-131. doi:10.3233/DMA-2011-0866 [doi]

Galbraith, S. M. (2006). MR in oncology drug development. *NMR in Biomedicine, 19*(6), 681-689. doi:10.1002/nbm.1093 [doi]

Gandhi, D., Chepeha, D. B., Miller, T., Carlos, R. C., Bradford, C. R., Karamchandani, R., . . . Mukherji, S. K. (2006). Correlation between initial and early follow-up CT perfusion parameters with endoscopic tumor response in patients with advanced squamous cell carcinomas of the oropharynx treated with organ-preservation therapy. *AJNR.American Journal of Neuroradiology, 27*(1), 101-106. doi:27/1/101 [pii]

Giesel, F. L., Bischoff, H., von Tengg-Kobligk, H., Weber, M. A., Zechmann, C. M., Kauczor, H. U., & Knopp, M. V. (2006). Dynamic contrast-enhanced MRI of malignant pleural mesothelioma: A feasibility study of noninvasive assessment, therapeutic follow-up, and possible predictor of improved outcome. *Chest, 129*(6), 1570-1576. doi:10.1378/chest.129.6.1570

Giesel, F. L., Choyke, P. L., Mehndiratta, A., Zechmann, C. M., von Tengg-Kobligk, H., Kayser, K., . . . Knopp, M. V. (2008). Pharmacokinetic analysis of malignant pleural mesothelioma-initial results of tumor microcirculation and its correlation to microvessel density (CD-34). *Academic Radiology, 15*(5), 563-570. doi:10.1016/j.acra.2007.12.014 [doi]

Gill, R. R., Umeoka, S., Mamata, H., Tilleman, T. R., Stanwell, P., Woodhams, R., . . . Hatabu, H. (2010). Diffusion-weighted MRI of malignant pleural mesothelioma: Preliminary assessment of apparent diffusion coefficient in histologic subtypes. *AJR.American Journal of Roentgenology, 195*(2), W125-30. doi:10.2214/AJR.09.3519

Gordon, Y., Partovi, S., Muller-Eschner, M., Amarteifio, E., Bauerle, T., Weber, M. A., . . . Rengier, F. (2014). Dynamic contrast-enhanced magnetic resonance imaging: Fundamentals and application to the evaluation of the peripheral perfusion. *Cardiovascular Diagnosis and Therapy, 4*(2), 147-164. doi:10.3978/j.issn.2223-3652.2014.03.01 [doi]

Heilmann, M., Kiessling, F., Enderlin, M., & Schad, L. R. (2006). Determination of pharmacokinetic parameters in DCE MRI: Consequence of nonlinearity between contrast agent concentration and signal intensity. *Investigative Radiology, 41*(6), 536-543. doi:10.1097/01.rli.0000209607.99200.53 [doi]

Kershaw, L. E., & Cheng, H. L. (2010). Temporal resolution and SNR requirements for accurate DCE-MRI data analysis using the AATH model. *Magnetic Resonance in Medicine, 64*(6), 1772-1780. doi:10.1002/mrm.22573 [doi]

Khalil, A., Majlath, M., Gounant, V., Hess, A., Laissy, J. P., & Debray, M. P. (2016). Contribution of magnetic resonance imaging in lung cancer imaging. *Diagnostic and Interventional Imaging, 97*(10), 991-1002. doi:S2211-5684(16)30215-7 [pii]

Kiessling, F., Jugold, M., Woenne, E. C., & Brix, G. (2007). Non-invasive assessment of vessel morphology and function in tumors by magnetic resonance imaging. *European Radiology, 17*(8), 2136-2148. doi:10.1007/s00330-006-0566-x [doi]

Koh, T. S., Bisdas, S., Koh, D. M., & Thng, C. H. (2011). Fundamentals of tracer kinetics for dynamic contrast-enhanced MRI. *Journal of Magnetic Resonance Imaging : JMRI, 34*(6), 1262-1276. doi:10.1002/jmri.22795; 10.1002/jmri.22795

Kovac, V., Zwitter, M., Rajer, M., Marin, A., Debeljak, A., Smrdel, U., & Vrankar, M. (2012). A phase II trial of low-dose gemcitabine in a prolonged infusion and cisplatin for malignant pleural mesothelioma. *Anti-Cancer Drugs, 23*(2), 230-238. doi:10.1097/CAD.0b013e32834d7a1c; 10.1097/CAD.0b013e32834d7a1c

Kulinna-Cosentini, C., Schima, W., & Cosentini, E. P. (2007). Dynamic MR imaging of the gastroesophageal junction in healthy volunteers during bolus passage. *Journal of Magnetic Resonance Imaging : JMRI, 25*(4), 749-754. doi:10.1002/jmri.20868 [doi]

Ledsam, J. R., Hodgson, R., Moots, R. J., & Sourbron, S. P. (2013). Modeling DCE-MRI at low temporal resolution: A case study on rheumatoid arthritis. *Journal of Magnetic Resonance Imaging : JMRI, 38*(6), 1554-1563. doi:10.1002/jmri.24061 [doi]

Mason, J., Broaddus, V., Martin, T., King, T., & Schraufnagel, D. (2010). Asbestos-related fibrosis of the lung (asbestosis) and pleura. *Murray and nadel's textbook of respiratory medicine* () Elsevier.

Naish, J. H., Kershaw, L. E., Buckley, D. L., Jackson, A., Waterton, J. C., & Parker, G. J. (2009). Modeling of contrast agent kinetics in the lung using T1-weighted dynamic contrast-enhanced MRI. *Magnetic Resonance in Medicine, 61*(6), 1507-1514. doi:10.1002/mrm.21814 [doi]

Nishino, M., Hatabu, H., Johnson, B. E., & McLoud, T. C. (2014). State of the art: Response assessment in lung cancer in the era of genomic medicine. *Radiology, 271*(1), 6-27. doi:10.1148/radiol.14122524 [doi]

Ohta, Y., Shridhar, V., Bright, R. K., Kalemkerian, G. P., Du, W., Carbone, M., . . . Pass, H. I. (1999). VEGF and VEGF type C play an important role in angiogenesis and lymphangiogenesis in human malignant mesothelioma tumours. *British Journal of Cancer, 81*(1), 54-61. doi:10.1038/sj.bjc.6690650 [doi]

Padhani, A. R., Hayes, C., Assersohn, L., Powles, T., Makris, A., Suckling, J., . . . Husband, J. E. (2006). Prediction of clinicopathologic response of breast cancer to primary chemotherapy at contrast-enhanced MR imaging: Initial clinical results. *Radiology, 239*(2), 361-374. doi:2392021099 [pii]

Padhani, A. R., & Khan, A. A. (2010). Diffusion-weighted (DW) and dynamic contrast-enhanced (DCE) magnetic resonance imaging (MRI) for monitoring anticancer therapy. *Targeted Oncology, 5*(1), 39-52. doi:10.1007/s11523-010-0135-8

Podobnik, J., Kocijancic, I., Kovac, V., & Sersa, I. (2010). 3T MRI in evaluation of asbestos-related thoracic diseases - preliminary results. *Radiology and Oncology, 44*(2), 92-96. doi:10.2478/v10019-010-0027-7 [doi]

Robinson, B. W., & Lake, R. A. (2005). Advances in malignant mesothelioma. *The New England Journal of Medicine, 353*(15), 1591-1603. doi:10.1056/NEJMra050152

Robinson, B. W., Musk, A. W., & Lake, R. A. (2005). Malignant mesothelioma. *Lancet, 366*(9483), 397-408. doi:10.1016/S0140-6736(05)67025-0

Roe, O. D., & Stella, G. M. (2015). Malignant pleural mesothelioma: History, controversy and future of a manmade epidemic. *European Respiratory Review : An Official Journal of the European Respiratory Society, 24*(135), 115-131. doi:24/135/115 [pii]

Ruffie, P., Feld, R., Minkin, S., Cormier, Y., Boutan-Laroze, A., Ginsberg, R., . . . Figueredo, A. (1989). Diffuse malignant mesothelioma of the pleura in ontario and quebec: A retrospective study of 332 patients. *Journal of Clinical Oncology : Official Journal of the American Society of Clinical Oncology, 7*(8), 1157-1168.

Rusch, V. W. (1995). A proposed new international TNM staging system for malignant pleural mesothelioma. from the international mesothelioma interest group. *Chest, 108*(4), 1122-1128.

Saddoughi, S. A., Abdelsattar, Z. M., & Blackmon, S. H. (2018). National trends in the epidemiology of malignant pleural mesothelioma: A national cancer data base study. *The Annals of Thoracic Surgery, 105*(2), 432-437. doi:S0003-4975(17)31320-6 [pii]

Scherpereel, A., Astoul, P., Baas, P., Berghmans, T., Clayson, H., de Vuyst, P., . . . European Respiratory Society/European Society of Thoracic Surgeons Task Force. (2010). Guidelines of the european respiratory society and the european society of thoracic surgeons for the management of malignant pleural mesothelioma. *The European Respiratory Journal : Official Journal of the European Society for Clinical Respiratory Physiology, 35*(3), 479-495. doi:10.1183/09031936.00063109; 10.1183/09031936.00063109

Scherpereel, A., Astoul, P., Baas, P., Berghmans, T., Clayson, H., de Vuyst, P., . . . European Society of Thoracic Surgeons. (2010). Guidelines of the european respiratory society and the european society of thoracic surgeons for the management of malignant pleural mesothelioma. *Zhongguo Fei Ai Za Zhi = Chinese Journal of Lung Cancer, 13*(10), C23-45. doi:10.3779/j.issn.1009-3419.2010.10.14 [doi]

Shen, Y., Goerner, F. L., Snyder, C., Morelli, J. N., Hao, D., Hu, D., . . . Runge, V. M. (2015). T1 relaxivities of gadolinium-based magnetic resonance contrast agents in human whole blood at 1.5, 3, and 7 T. *Investigative Radiology,* doi:10.1097/RLI.0000000000000132 [doi]

Sobin, L. H., Gospodarowicz, M. K., & Wittekind, C. (Eds.). (2009). *TNM classification of malignant tumours, 7th edition* (7th ed.) Wiley-Blackwell.

Sorensen, A. G., Emblem, K. E., Polaskova, P., Jennings, D., Kim, H., Ancukiewicz, M., . . . Jain, R. K. (2012). Increased survival of glioblastoma patients who respond to antiangiogenic therapy with elevated blood perfusion. *Cancer Research, 72*(2), 402-407. doi:10.1158/0008-5472.CAN-11-2464 [doi]

Sourbron, S. P., & Buckley, D. L. (2013). Classic models for dynamic contrast-enhanced MRI. *NMR in Biomedicine,* doi:10.1002/nbm.2940; 10.1002/nbm.2940

Stahel, R. A., Weder, W., Felip, E., & ESMO Guidelines Working Group. (2008). Malignant pleural mesothelioma: ESMO clinical recommendations for diagnosis, treatment and follow-up. *Annals of Oncology : Official Journal of the European Society for Medical Oncology / ESMO, 19 Suppl 2*, ii43-4. doi:10.1093/annonc/mdn083 [doi]

Strizzi, L., Catalano, A., Vianale, G., Orecchia, S., Casalini, A., Tassi, G., . . . Procopio, A. (2001). Vascular endothelial growth factor is an autocrine growth factor in human malignant mesothelioma. *The Journal of Pathology, 193*(4), 468-475. doi:10.1002/path.824 [pii]

Tofts, P. S., Brix, G., Buckley, D. L., Evelhoch, J. L., Henderson, E., Knopp, M. V., . . . Weisskoff, R. M. (1999). Estimating kinetic parameters from dynamic contrast-enhanced T(1)-weighted MRI of a diffusable tracer: Standardized quantities and symbols. *Journal of Magnetic Resonance Imaging : JMRI, 10*(3), 223-232. doi:10.1002/(SICI)1522-2586(199909)10:33.0.CO;2-S [pii]

Tudorica, A., Oh, K. Y., Chui, S. Y., Roy, N., Troxell, M. L., Naik, A., . . . Huang, W. (2016). Early prediction and evaluation of breast cancer response to neoadjuvant

chemotherapy using quantitative DCE-MRI. *Translational Oncology, 9*(1), 8-17. doi:10.1016/j.tranon.2015.11.016 [doi]

van Zandwijk, N., Clarke, C., Henderson, D., Musk, A. W., Fong, K., Nowak, A., . . . Penman, A. (2013). Guidelines for the diagnosis and treatment of malignant pleural mesothelioma. *Journal of Thoracic Disease, 5*(6), E254-307. doi:10.3978/j.issn.2072-1439.2013.11.28 [doi]

Vivoda Tomšič, M., & Podkrajšek, M. (2017). Dynamic MR imaging of pelvic floor dysfunction. *Appl Radiol., 46*(8), 21-27.

Vivoda Tomsic, M., Bisdas, S., Kovac, V., Sersa, I., & Surlan Popovic, K. (2019). Dynamic contrast-enhanced MRI of malignant pleural mesothelioma: A comparative study of pharmacokinetic models and correlation with mRECIST criteria. *Cancer Imaging : The Official Publication of the International Cancer Imaging Society, 19*(1), 10-019-0189-5. doi:10.1186/s40644-019-0189-5 [doi]

Vogelzang, N. J., Rusthoven, J. J., Symanowski, J., Denham, C., Kaukel, E., Ruffie, P., . . . Paoletti, P. (2003). Phase III study of pemetrexed in combination with cisplatin versus cisplatin alone in patients with malignant pleural mesothelioma. *Journal of Clinical Oncology : Official Journal of the American Society of Clinical Oncology, 21*(14), 2636-2644. doi:10.1200/JCO.2003.11.136

Wang, Z. J., Reddy, G. P., Gotway, M. B., Higgins, C. B., Jablons, D. M., Ramaswamy, M., . . . Webb, W. R. (2004). Malignant pleural mesothelioma: Evaluation with CT, MR imaging, and PET. *Radiographics : A Review Publication of the Radiological Society of North America, Inc, 24*(1), 105-119. doi:10.1148/rg.241035058

Wasser, K., Klein, S. K., Fink, C., Junkermann, H., Sinn, H. P., Zuna, I., . . . Delorme, S. (2003). Evaluation of neoadjuvant chemotherapeutic response of breast cancer using dynamic MRI with high temporal resolution. *European Radiology, 13*(1), 80-87. doi:10.1007/s00330-002-1654-1 [doi]

Westbrook.C. (2005). In Rooth.C.C., Talbot.J. (Eds.), *MRI in practice* (third ed.). Cambridge, UK: Blackwell Publishing.

Yu, H. J., Chen, J. H., Mehta, R. S., Nalcioglu, O., & Su, M. Y. (2007). MRI measurements of tumor size and pharmacokinetic parameters as early predictors of response in breast cancer patients undergoing neoadjuvant anthracycline chemotherapy. *Journal of Magnetic Resonance Imaging : JMRI, 26*(3), 615-623. doi:10.1002/jmri.21060 [doi]

Zadnik V, primic žakelj M. SLORA: Slovenija in rak. epidemiologija in register raka. onkološki inštitut ljubljana. web site www.slora.si. published december 2014. accessed july 9, 2015.

Zahid, I., Sharif, S., Routledge, T., & Scarci, M. (2011). What is the best way to diagnose and stage malignant pleural mesothelioma? *Interactive Cardiovascular and Thoracic Surgery, 12*(2), 254-259. doi:10.1510/icvts.2010.255893

Zalcman, G., Mazieres, J., Margery, J., Greillier, L., Audigier-Valette, C., Moro-Sibilot, D., . . . French Cooperative Thoracic Intergroup (IFCT). (2016). Bevacizumab for newly diagnosed pleural mesothelioma in the mesothelioma avastin cisplatin pemetrexed study (MAPS): A randomised, controlled, open-label, phase 3 trial. *Lancet (London, England), 387*(10026), 1405-1414. doi:S0140-6736(15)01238-6 [pii]

Zwitter, M., Kovac, V., Rajer, M., Vrankar, M., & Smrdel, U. (2010). Two schedules of chemotherapy for patients with non-small cell lung cancer in poor performance status: A phase II randomized trial. *Anti-Cancer Drugs, 21*(6), 662-668. doi:10.1097/CAD.0b013e32833ab7a0 [doi]

Bibliography

Publications Related to the Thesis

Journal Articles

Vivoda Tomsic, M., Bisdas, S., Kovac, V., Sersa, I., & Surlan Popovic, K. (2019). Dynamic contrast-enhanced MRI of malignant pleural mesothelioma: A comparative study of pharmacokinetic models and correlation with mRECIST criteria. *Cancer Imaging : The Official Publication of the International Cancer Imaging Society, 19*(1), 10-019-0189-5. doi:10.1186/s40644-019-0189-5

Vivoda Tomšič, M., & Podkrajšek, M. (2017). Dynamic MR imaging of pelvic floor dysfunction. *Appl Radiol., 46*(8), 21-27.

Conference Paper

Vivoda Tomšič, Martina, Šurlan Popović, Katarina, Bisdas, Sotirios, Kovač, Viljem, Serša, Igor. Dynamic contrast-enhanced MRI of malignant pleural mesothelioma : a comparative study of pharmacokinetic models and correlation with mRECIST criteria. Insights into imaging, ISSN 1869-4101, Mar. 2016, vol. 7, suppl. 1, str. S230. http://link.springer.com/article/10.1007/s13244-016-0475-8. [COBISS.SI-ID 2820268]

Biography

I was born on 1 September 1985 in Rijeka, Croatia, where I finished elementary and high school. In the third year of high school, I took part in an exchange program and attended the G. Ray Bodley School, Fulton, NY, USA.

I continued the studies at the Medical Faculty, University of Ljubljana, where I graduated on 29 April 2010. From 1 August 2010 until 31 January 2011 I was an intern at the University Medical Centre Ljubljana. After passing the state qualifying exam, I was a student fellow for 4 months at the Radiology Department at the San Raffaele Hospital in Milan, Italy. I started the specialization in radiology on 1 October 2011 at the University Medical Centre Ljubljana and I have successfully completed it on 30 September 2016. Since then, I have been working as a radiologist at the University Clinic of Pulmonary and Allergic Diseases Golnik.

My subspecialty fields are lung diseases and lung carcinomas. Apart from interpreting x-ray, ultrasound and computer tomography examinations, I also perform CT and ultrasound-guided cytological and histological biopsies and take part at the multidisciplinary tumor board and multidisciplinary interstitial lung disease board.

I am a member of the Slovenian Association of Radiology, European Society of Radiology (ESR), European Society of Thoracic Imaging (ESTI) and European Society of Oncology Imaging (ESOI).

In 2019, I have been elected as an assistant at the Medical Faculty of Ljubljana. I am also a direct mentor for radiology residents.